

LA

NASA  
Technical  
Paper  
2534

March 1986

Static Investigation of  
Circular-to-Rectangular  
Transition Ducts for  
High-Aspect-Ratio  
Nonaxisymmetric Nozzles

James R. Burley II,  
Linda S. Bangert,  
and John R. Carlson

{NASA-TP-2534} STATIC INVESTIGATION OF N86-22576  
CIRCULAR-TO-RECTANGULAR TRANSITION DUCTS FOR  
HIGH-ASPECT-RATIO NONAXISYMMETRIC NOZZLES  
{NASA} 55 p HC A04/MF A01 CSCL 21E Unclas  
H1/07 04134



**NASA**  
**Technical**  
**Paper**  
**2534**

1986

Static Investigation of  
Circular-to-Rectangular  
Transition Ducts for  
High-Aspect-Ratio  
Nonaxisymmetric Nozzles

James R. Burley II,  
Linda S. Bangert,  
and John R. Carlson

*Langley Research Center*  
*Hampton, Virginia*

**NASA**

National Aeronautics  
and Space Administration

Scientific and Technical  
Information Branch

## Summary

An investigation was conducted in the static-test facility of the Langley 16-Foot Transonic Tunnel to determine the overall internal performance of a high-aspect-ratio nonaxisymmetric nozzle and circular-to-rectangular transition ducts. Five transition ducts were used to explore the effects of duct length, wall shape, and cross-sectional area distribution on performance. In addition, one duct was tested with swirl vanes in an attempt to model the rotating flow inside a turbojet engine. Nozzle pressure ratio was varied from 1.5 to 5.3, and nozzle performance parameters were measured and recorded at steady-state conditions. The results indicate that overall performance of the transition duct and nozzle decreased when the transition-duct length was reduced from one entrance-plane diameter to one-half entrance-plane diameter. Discharge coefficient decreased 1 percent, and thrust ratio was reduced 0.5 percent. For duct lengths of 0.75 diameter and less, large regions of separated flow were observed inside the transition duct. These large regions indicated potentially severe wall cooling problems. While the straight and curved wall shapes investigated had no significant effect on performance, reducing the cross-sectional area of the duct improved overall performance and reduced flow separation. The swirl-vane results required significant assumptions during analysis and were considered inconclusive. Numerical results from the potential flow code MCAERO were used to predict the ratios of the internal static pressure to jet total pressure along the walls of the transition ducts. The calculated pressures did not accurately match the experimental data because of the highly viscous nature of the flow inside the transition ducts.

## Introduction

The need for innovative jet-engine exhaust systems with multifunction capability is being met by various nonaxisymmetric nozzle concepts (ref. 1). However, the rectangular shape of the nozzle has created the design problem of transitioning the axisymmetric engine flow to the nonaxisymmetric flow in the nozzle. The transition section, or duct as it is referred to in this paper, connects the axisymmetric engine to the nonaxisymmetric nozzle through a smooth progression of geometrically similar cross sections. The duct must be as short as possible to minimize the weight of the propulsion system installation. It must also be long enough to prevent any flow separation, which could adversely affect performance and create severe wall cooling problems. The cooling problem arises because most turbojet engines

rely on a thin film of cool air injected parallel to the walls to maintain temperatures within thermal limits. Flow separation causes the cool air to mix with the hot gases from the engine and then magnifies the problem by concentrating the hot gases at one or more stagnation points along the wall. Although this investigation was conducted with a cold jet, the separation patterns observed are directly applicable to full-scale engines with hot-exhaust jets. In addition to duct length, wall shape and cross-sectional area are expected to influence flow separation and performance.

Swirl vanes may help alleviate some flow separation by imparting a radial component to the velocity vectors, but more importantly, they can be used to reduce the noise associated with the jet exhaust (ref. 2). As shown in reference 3, swirling the flow will increase the rate of decay in the axial velocity component of the jet with minimal loss of thrust. However, references 2 and 3 are applicable to axisymmetric nozzles only. This investigation should provide information on the effects of swirl in nonaxisymmetric nozzles.

Because of the interest in multifunction nonaxisymmetric nozzles and the possibility of significant internal performance losses due to the high-aspect-ratio transition duct and flow swirl, the present investigation was undertaken to experimentally examine transition-duct design. Five transition ducts were used to explore the effects of duct length, wall shape, and cross-sectional area distribution on performance. The investigation was conducted in the static-test facility of the Langley 16-Foot Transonic Tunnel at static conditions. Nozzle pressure ratio was varied from 1.5 to 5.3, and nozzle performance parameters were measured and recorded at steady-state conditions. Static pressures were measured inside each transition duct and used as diagnostic aids in explaining and understanding the flow behavior inside the duct. Flow-visualization photographs were taken of selected transition ducts and were used to support and clarify the static-pressure data. For the baseline configuration, the total-pressure profiles at the entrance and exit of the duct were integrated to obtain the total-pressure loss through the duct. Finally, numerical calculations of the transition-duct wall static pressures were compared with the experimental data.

## Symbols and Abbreviations

$A_{cs}$	cross-sectional area, in <sup>2</sup>
$A_e$	nozzle exit area, in <sup>2</sup>
$A_t$	nozzle throat area, in <sup>2</sup>
AR	aspect ratio (width/height)

$a$	semimajor axis length, in.
$b$	semiminor axis length, in.
$C_p$	static-pressure coefficient, $\frac{p-p_\infty}{p_\infty}$
Conf.	configuration
$d$	transition-duct entrance diameter, 5.064 in.
$F$	measured thrust along body axis, lbf
$F_i$	ideal isentropic gross thrust, $W_p \sqrt{\frac{RT_{t,j}}{g} \left( \frac{2\gamma}{\gamma-1} \right) \left( 1 - \frac{p_\infty}{p_{t,j}} \right)^{(\gamma-1)/\gamma}}, \text{ lbf}$
$F/F_i$	thrust ratio
$g$	gravitational constant, 32.174 ft/sec <sup>2</sup>
$h$	height of transition-duct exit plane, in.
$l$	transition-duct length, in.
$l_n$	nozzle length, in.
$M_j$	jet Mach number
NPR	nozzle pressure ratio, $p_{t,j}/p_\infty$
$p$	local static pressure, psia
$p_{t,j}$	jet total pressure, psia
$p_\infty$	ambient pressure, psia
$P_{1-5}$	pressure orifices on probe (see fig. 6)
$R$	gas constant, ft-lbf/lbm °R
$r$	transition-duct entrance radius, 2.532 in.
Sta.	model station, in.
$T_{t,j}$	jet total temperature, °R
$t$	dummy variable of integration (see eq. (A3))
$W_i$	ideal isentropic weight-flow rate, lbf/sec
$W_p$	measured weight-flow rate, lbf/sec
$W_p/W_i$	discharge coefficient
$w$	width of transition-duct exit plane, in.
$x$	axial distance from transition-duct entrance, in.
$y$	coordinate of transition duct measured laterally from model centerline, in.
$z$	coordinate of transition duct measured vertically from model centerline, in.
$\alpha_1$	maximum slope angle of transition sidewalls, $\tan^{-1}  dy/dx $ at $x/l = 0.5$ , deg

$\alpha_2$	maximum slope angle of transition top or bottom walls, $\tan^{-1}  dz/dx $ at $x/l = 0.5$ , deg
$\Gamma$	Gamma function
$\gamma$	ratio of specific heats, 1.3997 for air
$\eta$	exponent in superellipse equation (see appendix)

## Apparatus and Procedure

### Static-Test Facility

The investigation was conducted in the static-test facility of the Langley 16-Foot Transonic Tunnel. The model testing bay has a high ceiling and a large open door for exhausting the jet to atmosphere. The model is operated from a remotely located control room and monitored by a television camera. An external high-pressure-air system provides weight flows up to 15 lbf/sec, and jet total temperature can be varied from 500°R to 600°R.

### Single-Engine Propulsion-Simulation System

The model support and air transfer system used in the static-test facility is identical to the axisymmetric single-engine propulsion simulator described on page 119 of reference 4. Figure 1 illustrates the basic components of the air transfer system. The high-pressure-air system provided a continuous flow of clean, dry air at a controlled temperature of about 530°R. The air was transferred across the balance through flexible metal bellows to minimize axial forces caused by momentum and pressurization. From the bellows, the air was passed into a low-pressure plenum and through a choke plate. Total pressure and temperature measured in the high-pressure plenum upstream of the bellows were used to compute exhaust weight flow  $W_p$ . Nozzle pressure ratio was set based on the average total pressure measured in the instrumentation section downstream of the choke plate.

### Model

The components of the transition-duct model are illustrated in figure 2. This assembly attaches to the single-engine propulsion-simulation system shown in figure 1 at model station 36.0. Principal components of this assembly are the instrumentation section where jet total pressure  $p_{t,j}$  and temperature  $T_{t,j}$  are measured, the swirl chamber (20° or 30° vane angle), the pressure box with transition duct inside, and the nonaxisymmetric nozzle. The pressure box is a rectangular pressure vessel of 0.5-in-thick steel

into which the aluminum transition-duct block is inserted. This design allowed several transition ducts to be built and tested in a common pressure vessel, thereby simplifying model changes and hardware design.

**Transition ducts.** The transition-duct design for a nonaxisymmetric nozzle installation involves many variables. For this investigation, it was decided that the transition from axisymmetric engine to nonaxisymmetric nozzle would take place through a series of superellipses. The procedure used in designing the transition ducts is explained in the appendix, and the resulting ducts are fully described by the variables listed in table I. Three parameters were selected for study because of their significant influence on transition-duct shape. They are transition length  $l$ , wall shape (straight versus curved), and cross-sectional area  $A_{cs}$  distribution (constant versus decreasing).

Figure 3 illustrates the differences in sidewall and topwall design for the five transition ducts tested. The effects of transition length on duct shape are shown in figure 3(a). Configurations 2, 3, and 4 had the same constant cross-sectional area distribution and curved wall-shape equation. The wall-shape equations are given in the appendix. The maximum wall angles  $\alpha_1$  and  $\alpha_2$  increased with decreasing transition-duct length and always occurred at  $x/l = 0.5$ . Reference 1 suggests limiting  $\alpha_1$  and  $\alpha_2$  to  $45^\circ$  or less to prevent flow separation. For this reason, duct lengths were chosen so that maximum wall angles above and below the suggested limit of reference 1 were explored. Values of  $\alpha_1$  and  $\alpha_2$  for all configurations are given in figure 3. Figure 3(b) shows the two different wall shapes investigated. The straight or linear wall shape of transition duct 1 was tested as an alternative to the third-order wall shape of configuration 2, because it represented a simpler design to build. Also, for configuration 1, the maximum wall angles were reduced in relation to configuration 2, although abrupt changes in wall slope were created at the entrance and exit of the transition duct. Cross-sectional area was held constant for configurations 1 through 4. Figure 3(c) illustrates the differences in design between the constant-area duct 2 and the reduced-area duct 5. Because it is impossible to vary the cross-sectional area of a transition duct without affecting other geometric parameters, configuration 5 does not address area distribution alone. The cross-sectional area was reduced 25 percent over the length of duct 5 in a linear manner, while the duct-exit aspect ratio was maintained at 6.33 (same as ducts 1 through 4). The maximum sidewall angle  $\alpha_1$  was set equal to the configuration-2

value of  $42.7^\circ$ . To do this, the length of duct 5 had to be reduced from  $1.00l/d$  to  $0.75l/d$  and  $\alpha_2$  had to be increased from  $25.9^\circ$  to  $34.5^\circ$ .

**Nozzles.** Two nozzles were designed with the same expansion ratio ( $A_e/A_t = 1.248$ ), divergent flap angle ( $5.38^\circ$ ), and throat aspect ratio ( $AR = 15$ ). Figure 4 presents the details of the nozzle designs. The first nozzle was tested with transition ducts 1 through 4, and the second nozzle was tested with duct 5. The reducing cross-sectional area distribution of duct 5 necessitated the second nozzle design. In both cases, the flow paths were sized to be representative of current aircraft propulsion-system installations, and both nozzles simulated dry-power operation.

**Swirl vanes.** Swirl was induced in the flow by a set of vanes ahead of the transition as shown in figure 2. Vane angles of  $20^\circ$  and  $30^\circ$  were tested. The swirl vanes consisted of 12 flat-plate blades inclined to the flow axis at  $20^\circ$  and  $30^\circ$  and attached to a central hub with a diameter of approximately 0.75 in.

### Instrumentation

Forces and moments acting on the model downstream of Sta. 20.50 were measured with a six-component strain-gage balance. Jet total pressure and temperature were measured in the instrumentation section with a five-probe pitot rake and a single thermocouple. Figure 5 shows the locations of the 50 static-pressure orifices located on the bottom half of each of the five transition ducts. The table in figure 5 gives the  $x/l$  and  $y/a$  locations of each orifice. The  $z/b$  orifice coordinate can be computed from the superellipse equation shown in figure 5. A single row of 10 orifices was located on the centerline of the nozzle lower flap and the table in figure 4 gives the location of each orifice. A map of the total pressure entering and exiting configuration 2 was drawn from measurements taken with the probe shown in figure 6. The probe head has five pressure orifices designed to measure total pressure, static pressure, and two flow angles. For this investigation, only the total-pressure orifice  $p_1$  was used. The right side of figure 6 shows the locations at which  $p_1$  was measured in the entrance plane ( $x/l = -0.05$ ) and exit plane ( $x/l = 1.05$ ) of configuration 2.

### Data Reduction

All data were recorded on magnetic tape at a rate of 10 frames per second for a period of 5 seconds. The average of the 50 frames was used in computations. Data were recorded as NPR was increased from 1.5

to 5.3. For the probe data, NPR was maintained at a nominal value of 4.0 while the probe was moved from station to station. All forces were referenced to the model centerline.

The basic performance parameter used for the presentation of results is the internal thrust ratio  $F/F_i$ , which is the ratio of the actual nozzle thrust (along the body axis) to the ideal nozzle thrust. The ideal thrust was computed from the isentropic flow equation and the measured weight flow  $W_p$ , and actual nozzle thrust was obtained from the balance axial-force measurement corrected for weight tares and balance interactions. Although the bellows arrangement was designed to eliminate pressure and momentum interactions with the balance, small bellows tares on axial, normal, and pitch balance components still exist. These tares result from a small pressure difference between the ends of the bellows when internal velocities are high and from small differences in the forward- and aft-bellows spring constants when the bellows are pressurized. As discussed in reference 5, these bellows tares were determined by running calibration nozzles with known performance over a range of expected normal forces and pitching moments. The balance data were then corrected in a manner similar to that discussed in reference 5.

## Results and Discussion

### Performance Data

The effects of transition length, wall shape, and area distribution without swirl are discussed in terms of how discharge coefficient and thrust ratio vary with NPR. Swirl-vane effects are shown for configuration 2 only. In all cases, the data reflect the overall performance of the nozzle and transition duct.

**Transition length.** Figure 7 illustrates the effect that changing transition length has on performance. With the transition-duct exit station fixed relative to the nozzle, the entrance plane moves closer to the nozzle with decreasing transition length. For configuration 4, this places the transition entrance only  $0.50l/d$  (approximately 2.5 in.) upstream of the nozzle. The rapid change from axisymmetric to non-axisymmetric flow had surprisingly little effect on performance for duct 4. Discharge coefficient was reduced 1 percent, and thrust ratio suffered only a 0.5 percent loss. Configuration 3 was an intermediate length of  $0.75l/d$  and experienced no loss in discharge coefficient; however, thrust ratio was slightly reduced. Overall, the performance was very good, even for the shortest transition duct (Conf. 4). The losses indicated were probably caused by flow separation

inside the transition duct. The subsequent discussions of pressure distributions and flow-visualization photographs address the flow-separation problem in more detail.

**Wall shapes.** The straight (Conf. 1) and curved (Conf. 2) wall shapes investigated are compared in figure 8. Both ducts were the same length and had the same constant cross-sectional area distribution. However, configuration 2 had greater maximum wall angles  $\alpha_1$  and  $\alpha_2$  than configuration 1. This may be why duct 1 performed slightly better than duct 2. The sharp edge at the entrance and exit of duct 1 was expected to cause significant losses, but, as figure 8 shows, this was not the case. It seems likely that the optimum wall shape lies somewhere between ducts 1 and 2, with lower values of  $\alpha_1$  and  $\alpha_2$  and smooth continuous sidewalls at the entrance and exit to the transition duct. However, the very small differences in performance between ducts 1 and 2 suggest that other factors, such as construction costs and design simplicity, may have a greater influence on wall shape design.

**Area distribution.** The performances of transition ducts 2 and 5 are compared in figure 9. The sidewall equation and  $\alpha_1$  were held constant for ducts 2 and 5. However, to do this the length of duct 5 had to be reduced to  $0.75l/d$ , and the cross-sectional area had to be linearly reduced by 25 percent. The previous discussion on transition-duct length indicated that a length of  $0.75l/d$  (duct 3) produced no appreciable change in performance. Therefore, it may be inferred that the data of figure 9 illustrate cross-sectional area effects only. The favorable pressure gradient established in duct 5 reduced flow separation, which led to a 1.5-percent improvement in discharge coefficient. Thrust ratio also improved, but to a lesser degree. Flow-visualization photographs which show the reduction in separation are presented subsequently and are discussed in the section entitled "Flow Visualization."

**Swirl vanes.** Figure 10 shows the effect of swirl on discharge coefficient and thrust ratio for configuration 2. The swirl vanes were located downstream of the jet total-pressure rake, and, because of the total-pressure loss caused by the vanes, two assumptions had to be made during calibrations to reduce the data of figure 10. The Stratford convergent axisymmetric nozzle used as a weight-flow standard was tested with and without swirl. This nozzle had no pressure instrumentation, so the total-pressure loss across the swirl vanes could not be determined. Therefore,

to reduce the data, it was assumed that the total-pressure loss across the vanes was zero and that the known discharge coefficient and thrust ratio of the Stratford nozzle was unaffected by the swirling flow. Based on these assumptions, the data of figure 10 show no effect of swirl on discharge coefficient and show a loss in thrust ratio due to the presence of the swirl vanes. If the total-pressure loss across the swirl vanes were accurately measured with the Stratford convergent axisymmetric nozzle installed, the blockage caused by the vanes could be removed from the data and would leave only the effects of swirl. Theoretical calculations performed in reference 6 on a convergent axisymmetric nozzle indicate a loss of 7 to 8 percent in discharge coefficient and a 1- to 2-percent loss in thrust ratio for a swirl-vane angle of  $40^\circ$ . No results of any kind could be found that illustrated the effects of swirl on the performance of a nonaxisymmetric nozzle. Further calibrations are required in order to analyze the effects of swirl on the current data.

### Pressure Data

The static-pressure data are plotted against orifice location in figure 11. These data were used to construct figures 12 through 14. The static pressure  $p$  at each orifice location is nondimensionalized by the jet total pressure  $p_{t,j}$  and is referred to as the static-pressure ratio. Each symbol represents a different location of  $x/l$  as identified on the right-hand side of figure 11. Data are plotted at a nominal NPR of 3.18 for all transition ducts with and without swirl. The isobars presented in figures 12, 13, and 14 were drawn with the software package described in reference 7.

**NPR effects.** Figure 12 presents the effect of NPR on static-pressure ratios for configuration 4. Three values of NPR are shown in two different formats. On the right-hand side are contours of  $p/p_{t,j}$  with NPR increasing from bottom to top. On the left-hand side,  $p/p_{t,j}$  is plotted against  $x/l$  for the sidewall and bottom-wall distributions. In general, static pressures in the transition duct decrease with increasing NPR. The unfavorable pressure gradient along the sidewall of configuration 4 leads to flow separation at approximately  $x/l = 0.25$  for all three values of NPR. Along the bottom wall, the flow is accelerated under the influence of a favorable pressure gradient and shows no signs of separation.

**Swirl vanes.** Figure 13 illustrates the effect of swirl-vane angle on the static-pressure-ratio contours in transition duct 4. The flow is from top to bottom,

and the important thing to notice is that the symmetrical pattern with no swirl becomes unsymmetrical when the swirl vanes are added. Similar patterns were observed in all five transition ducts and on the top half of each duct.

**Total-pressure profiles.** Total-pressure-ratio contours at the entrance and exit planes of transition duct 2 are shown in figure 14 with and without swirl at a nominal NPR of 4.24. The data were area weighted and integrated to determine the average total pressure, so that total-pressure losses through the transition duct could be determined. For configuration 2 without swirl, there was no measurable loss in total pressure. With  $30^\circ$  swirl, there was a 7-percent reduction in average total pressure at the entrance station relative to the no-swirl data. Again, there was no measurable loss in total pressure through the transition duct. The total-pressure probe could not be positioned as close to the walls as desired. For this reason, the viscous layer near the wall where losses were most likely to occur was not included in the pressure-area integration and so no total pressure losses were detected. The contours of figure 14 indicate a significant change in the total pressure field when swirl is added. Without the swirl vanes, the total pressure is uniform across the entrance and exit planes. With swirl, the wake from the hub of the vanes can be seen in the inlet total pressure field and in the exit total pressure field although visibly decayed. Although the wake has decayed, no significant change has taken place in the shape of the contours due to the transition from axisymmetric to nonaxisymmetric flow.

### Flow Visualization

To visualize the flow, a mixture of 90-weight oil and carbon powder was painted on the interior surface of each transition duct. The photographs were taken by removing the nozzle after operating the jet and looking directly upstream into the transition duct. Because of the shape of the transition ducts, only the sidewalls were visible; however, this was the area of greatest interest.

Oil-flow photographs of configuration 4 with  $30^\circ$ -swirl vanes are presented in figure 15. Small arrows are superimposed on the sidewall photographs to indicate flow direction. The region of separated flow which begins at  $x/l = 0.25$  is probably responsible for the performance losses noted previously for configuration 4 in the discussion of transition-length effects. Photographs of the no-swirl and  $20^\circ$ -swirl configurations are not presented; however, they indicate the same separation patterns as the  $30^\circ$ -swirl configuration, except that the no-swirl case was symmetrical

about the centerline. It would seem that such a large separated region would have a severe impact on performance, but as figures 7 and 9 show, the overall effect was small. This small effect may be due in part to the length of the nozzle. A full-scale, fully integrated nozzle would be shorter in comparison. The long nozzle may provide the flow with enough time to reattach, so that no performance losses are measured. Without the extra length provided by the long nozzle, the separated flow shown in figure 15 would probably have a more pronounced effect on performance and would probably increase nozzle cooling requirements significantly.

The oil-flow photographs in figure 16 show why configuration 5 had the highest measured performance of all transition ducts tested. The flow appears to be well behaved, and no separation is apparent. There is no separation because of a favorable pressure gradient in the transition duct, which was caused by the decreasing cross-sectional area distribution of configuration 5.

## Theoretical Calculations

**Method description.** The numerical computations of the internal pressures were performed using the code MCAERO (ref. 8), a three-dimensional subsonic aerodynamic panel code which solves a set of linear potential-flow equations. All computations were made under the assumption that the flow was inviscid, irrotational, and incompressible, which allowed the flow to be described by the Laplace equation. The linearization of the equation, because of these assumptions, permits a superposition principle to be used to describe the flow about a body. The superposition of solutions for a second-order distribution of doublets upon the body surface describes the influence on the flow caused by the body. In the MCAERO analysis code, exterior and interior surfaces are described by an array of quadrilateral panels conforming to the body contours. The calculations performed herein were for purely internal flows. No compressibility corrections were included, and no corrections were made for viscous effects.

The numerical modeling of the duct consisted of inflow and outflow boundaries, an entrance section, and the transition duct and nozzle (fig. 17). The long entrance section reduces the influence of the transition duct on the uniformity of the flow at the inflow boundary. The velocities of the flow normal to the inflow and outflow faces were specified as boundary conditions. The velocities were required to satisfy the conservation of mass flow at the boundaries. The flow in the duct was subsonic up to the nozzle throat. This theoretical method does not model sonic flows;

therefore, the supersonic expansion downstream of the throat was not predicted.

The pressure coefficients calculated in MCAERO were converted to local static pressure divided by jet total pressure by using the following equation:

$$\frac{p}{p_{t,j}} = \left( \frac{\gamma M_j^2}{2} C_p + 1 \right) \left( 1 + \frac{M_j^2}{5} \right)^{-7/2}$$

Jet Mach number was determined by the ratio of the nozzle throat area to the entrance area of the transition duct, assuming choked flow conditions at the nozzle throat.

Comparisons of experimental data with numerical calculations are shown in figures 18 through 21. Sidewall and bottom-wall static pressures are compared with pressures calculated from MCAERO.

**Comparison for duct 2.** The theory accurately predicted the trends of the experimental wall pressures for duct 2. (See fig. 18.) The compression trend of the flow on the sidewall was predicted, but the actual level of pressure was too high. The expansion trend of the flow on the bottom wall was also predicted, and again the level was too high. The level discrepancy between the theory and experiment could be due to the mismatch of the inflow Mach number  $M_j$  used to convert the calculated pressure coefficients to static-pressure ratios.

The theory matched experiment well into the nozzle section, but could not accurately predict neither the choked flow conditions at the throat nor the supersonic expansion along the flaps because of limitations of the governing equations. Boundary-layer thickening would seem an unlikely cause for the level discrepancy seen in the transition duct, since the slopes of the theoretical and experimental curves match accurately for the complete length of the duct. An increasing boundary-layer thickness would change the effective shape of the wall that the flow would see and would therefore change the shape of the pressure distribution rather than just the level of the curve.

**Comparison for duct 3.** The theoretical predictions for duct 3 are presented in figure 19. The compression trend of the sidewall flow was predicted, but the slopes of the curves were not matched as well as for the duct-2 comparisons. The maximum sidewall angle was higher for duct 3 than for duct 2; therefore, boundary-layer effects such as rapid thickening or separation could cause these mismatches. The sidewall flow prediction closely matched the experimental data in the first 15 percent of the duct length but subsequently showed a compression trend more

rapid than the experimental data. Local boundary-layer thickening could decrease the apparent diverging angle of duct sidewalls. The flow velocity would change less rapidly with a less drastic wall geometry.

The expansion trend of the transition-duct bottom-wall flow was predicted. The theory was again high in overall level of pressure. The theory did predict the lower duct-exit static pressures for duct 3 in comparison with duct 2 ( $x/l = 0.95$ ). The comparison of predicted nozzle static-pressure ratios with experimental data shows a similar trend as was seen in the duct-2 comparison.

**Comparison for duct 4.** The comparison of theory versus experimental data for duct 4 is shown in figure 20. Prediction of the general compression trend of the sidewall flow was evident. As with duct 3, the level and trend of the static-pressure ratios in the first 15 percent of the duct were predicted. The match rapidly deteriorated after this point. The flow separated from the sidewall by  $x/l = 0.20$ , as was confirmed by the presence of a recirculation region in the flow-visualization photographs. Also, the duct walls were highly curved, and these rapid changes in panel slopes caused some numerical modeling difficulties as can be seen in the theoretical sidewall distribution at about  $x/l = 0.96$ .

The expansion trend of the flow along the bottom wall was, as before, predicted. Again, the theory predicted lower duct-exit static-pressure for duct 4 than for ducts 2 and 3 at  $x/l = 0.95$ . The predicted flow was slower, and a worse match of the slopes of the experimental data was seen. This mismatch was likely the result of stronger viscous effects. These effects were first evident in the duct-3 comparisons. Duct 4 had the highest wall divergence angle and the shortest duct length. These combined to cause very drastic flow phenomena that the present theory was unable to adequately predict.

**Comparison for duct 5.** The comparison of theory and experiment for duct 5 is presented in figure 21. The overall match of the theory with the experimental data was best for duct 5. The predicted level and trend matching were very good for both the sidewall and the bottom-wall pressure distributions, except for the nozzle throat areas. A factor contributing to the closer match could be

a better matching of the inflow Mach number, a problem that was mentioned in the discussion of the duct-2 comparison. An additional factor could be the different pressure gradient that exists in the duct because of the decreasing cross-sectional area. This more favorable pressure gradient would lessen boundary-layer growth and would therefore have less of an effect on the duct static pressures.

## Conclusions

An investigation was conducted in the static-test facility of the Langley 16-Foot Transonic Tunnel to determine the overall internal performance of a high-aspect-ratio nonaxisymmetric nozzle and circular-to-rectangular transition ducts. Five transition ducts were used to explore the effects of duct length, wall shape, and cross-sectional area distribution on performance. The results of this investigation indicate the following:

1. Overall performance was decreased when the duct length was reduced from one entrance-plane diameter to one-half entrance-plane diameter. Discharge coefficient decreased 1 percent, and thrust ratio was reduced 0.5 percent. For duct lengths of 0.75 diameters or less, large regions of separated flow were observed inside the duct. These regions indicated potentially severe wall cooling problems.
2. The straight and curved wall shapes investigated had no significant effect on performance, but only two shapes were tested and at only one duct length.
3. Reducing the cross-sectional area of the transition duct from the entrance to the exit by 25 percent improved overall performance and reduced flow separation.
4. The potential-flow code MCAERO was used to predict the ratios of internal static pressure to jet total pressure along the walls of the transition ducts. The numerical results did not accurately match the experimental data because of the highly viscous nature of the flow inside the transition ducts.

NASA Langley Research Center  
Hampton, VA 23665-5225  
November 25, 1985

## Appendix

### Method of Calculating Circular-to-Rectangular Transition Surfaces

James R. Burley II  
NASA Langley Research Center  
Hampton, Virginia

An interactive procedure has been developed and programmed for a digital computer to calculate the transition surface which connects a circular surface to a rectangular surface. The transition is formed by connecting a series of superellipse cross sections. The procedure requires that the cross-sectional area distribution and major and minor axes of the superellipses be defined. These are used as boundary conditions to solve for the shape of the transition. The procedure has been used to design aircraft forebodies, engine inlets, and internal ducts.

#### Technique

A circle, an ellipse, and a rectangle are all specific cases of superellipses. The locus of points which make up a superellipse is defined by the equation

$$(y/a)^\eta + (z/b)^\eta = 1 \quad (\text{A1})$$

Figure A1 shows a generalized superellipse in the  $y$ - $z$  plane with the semimajor and semiminor axes defined. Figure A2 illustrates the specific cases of superellipses, their properties, and the coordinate system used in this procedure. The area enclosed by the superellipse  $A_{cs}$  in figure A1 can be computed from the following equation (ref. 9):

$$A_{cs} = \frac{\Gamma(1/\eta)^2}{\Gamma(2/\eta)} (2/\eta)(4ab) \quad (\text{A2})$$

where  $\Gamma$  refers to the "gamma function" and is defined as

$$\Gamma(\eta) = \int_0^\infty (e^{-t} t^{\eta-1}) dt \quad (\eta > 0) \quad (\text{A3})$$

Calculation of the gamma function is addressed fully in reference 10.

With  $A_{cs}$ ,  $a$ , and  $b$  defined as continuous analytic functions of  $x$ , the transition surface is determined by iteratively computing  $\eta(x)$  from equation (A2). The relationship between  $A_{cs}/(ab)$  and  $\eta$  is illustrated in figure A3. For practical applications, a rectangle ( $\eta = \infty$ ) can be accurately approximated with  $\eta = 50$ .

#### Sample Calculation

To illustrate the procedure, an internal duct was designed which mated a circular duct to a rectangular duct with an exit aspect ratio (width/height) of 6.33. The results of the calculations are shown in figure A4. The transition duct shown in figure A4 is configuration 2 of the investigation reported in the body of this paper. The cross-sectional area  $A_{cs}$  was held constant through the duct, and the major and minor axes were constrained according to the equations

$$a(x) = r - (r - w)(x/l)^2[3 - 2(x/l)] \quad (\text{A4})$$

$$b(x) = r - (r - h)(x/l)^2[3 - 2(x/l)] \quad (\text{A5})$$

These equations have zero first derivatives with respect to  $x$  at  $x = 0$  and  $x = l$ ; therefore, a smooth transition is formed. As a result of the high aspect ratio of the transition-duct exit, the computed values of  $\eta$  in table I remain nearly constant ( $\eta \approx 2$ ) until  $x/l$  exceeds 0.75.

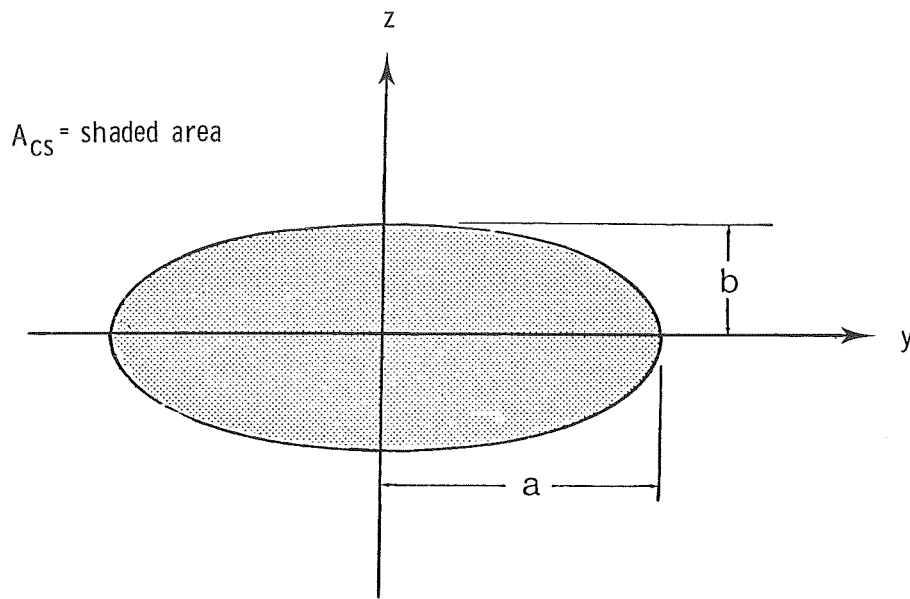


Figure A1. Typical cross section of a superellipse transition duct.

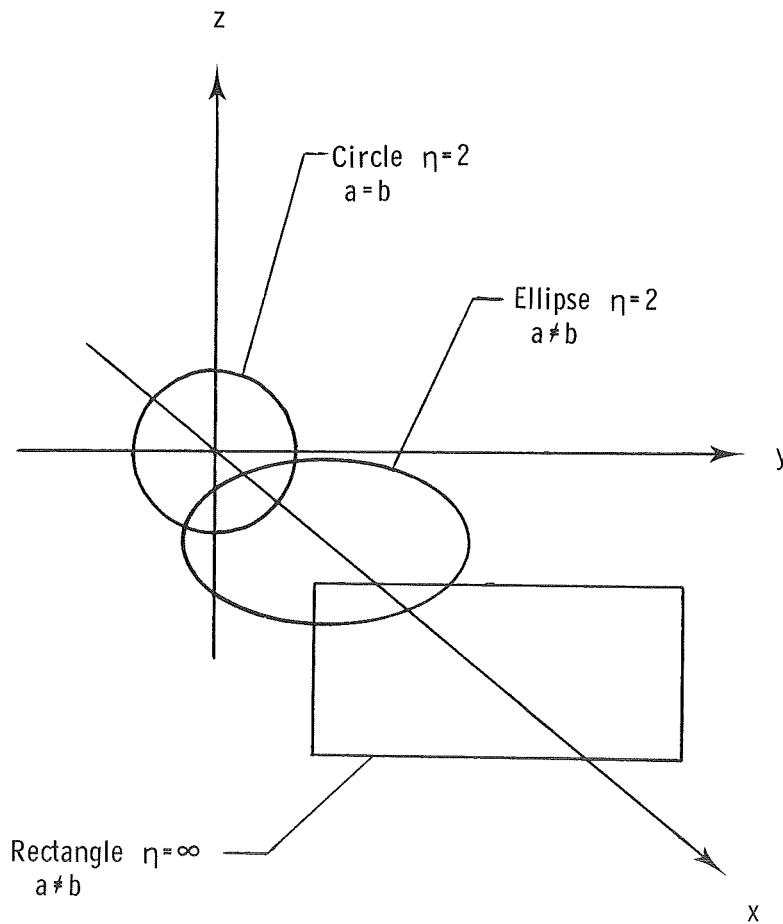


Figure A2. Specific cases of superellipses and coordinate-system orientation.

$$\lim_{\eta \rightarrow \infty} \left[ A_{CS}/(ab) \right] = 4$$

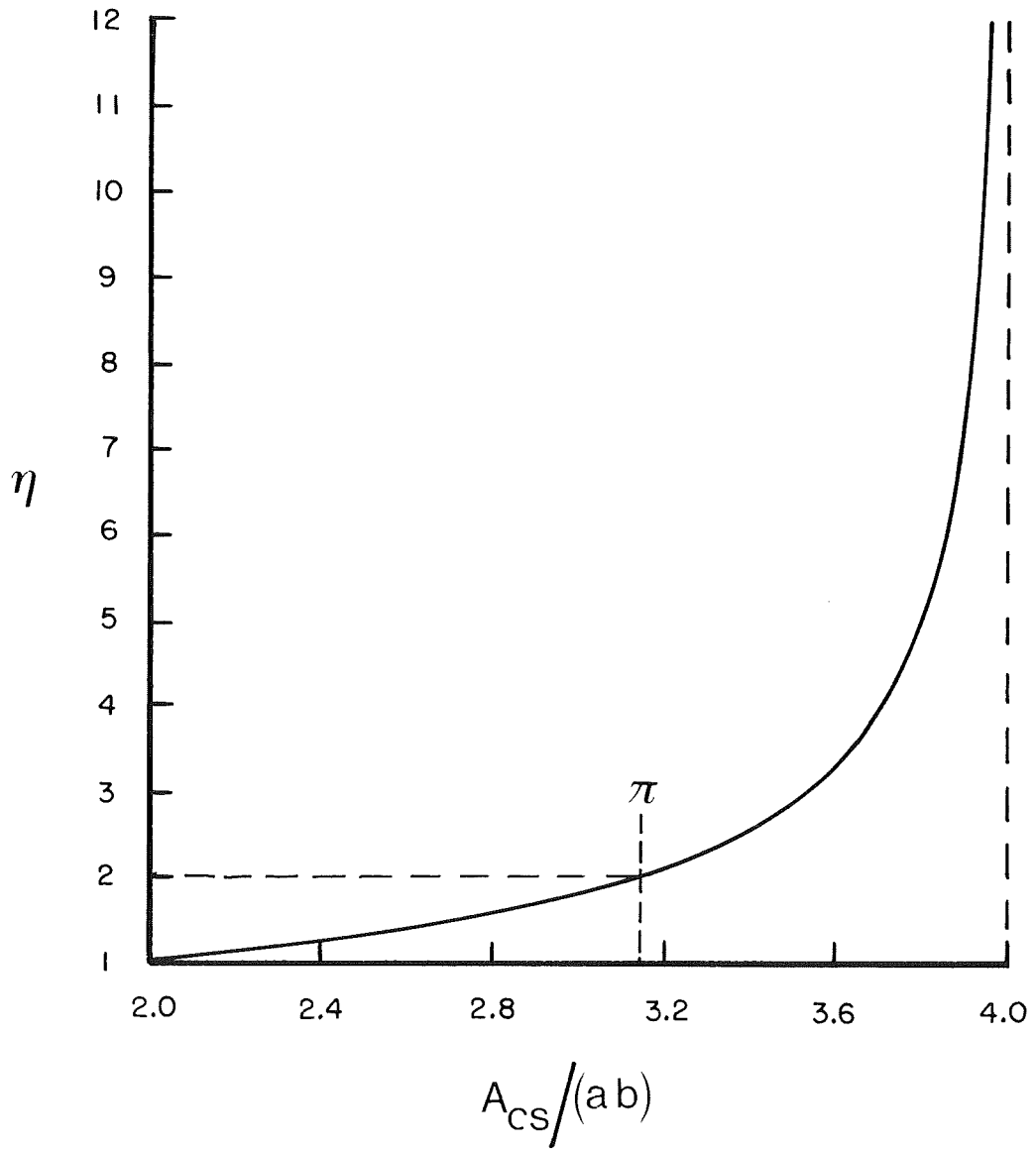


Figure A3. Variation of cross-sectional area with increasing values of superellipse exponent  $\eta$ .

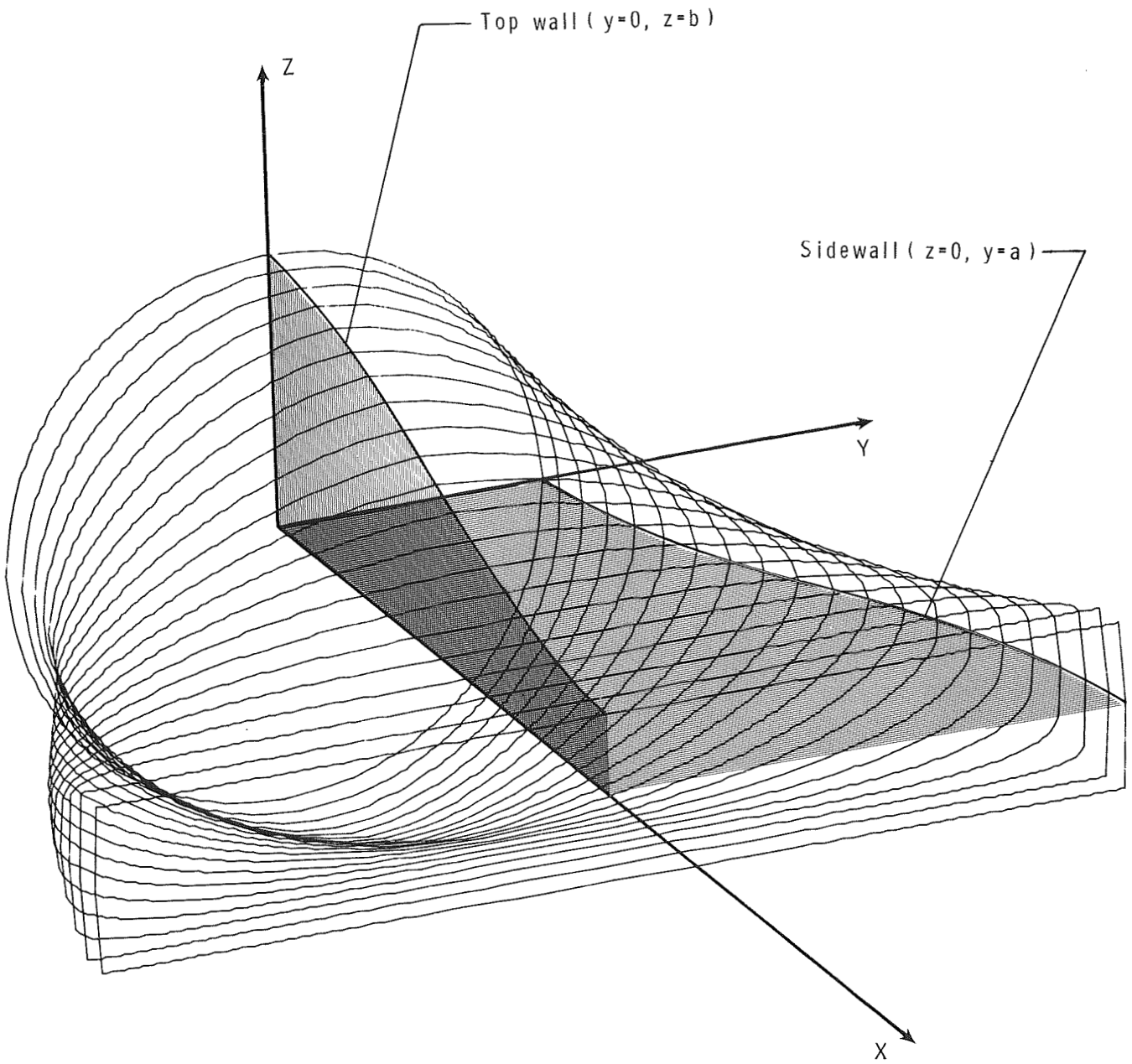


Figure A4. Analytical model of configuration-2 transition duct showing coordinate-system orientation and sidewall definitions.

## References

1. Stevens, H. L.; Thayer, E. B.; and Fullerton, J. F.: Development of the Multi-Function 2-D/C-D Nozzle. AIAA-81-1491, July 1981.
2. Schwartz, I. R.: Minimization of Jet and Core Noise of a Turbojet Engine by Swirling the Exhaust Flow. AIAA Paper 75-503, Mar. 1975.
3. Beer, J. M.; and Chigier, N. A.: *Combustion Aerodynamics*. Robert E. Krieger Publ. Co., 1983, pp. 100-146.
4. Peddrew, Kathryn H., compiler: *A User's Guide to the Langley 16-Foot Transonic Tunnel*. NASA TM-83186, 1981.
5. Capone, Francis J.: *Static Performance of Five Twin-Engine Nonaxisymmetric Nozzles With Vectoring and Reversing Capability*. NASA TP-1224, 1978.
6. Carpenter, P. W.: Effects of Swirl on the Subcritical Performance of Convergent Nozzles. *AIAA J.*, vol. 18, no. 5, May 1980, pp. 600-602.
7. Adams, Jeanne C.; Cline, Alan K.; Drake, Margaret A.; and Sweet, Roland A., eds.: NCAR Software Support Library, Volume 3. NCAR-TN/IA-105, Atmos. Technol. Div., Nat. Center Atmos. Res., Mar. 1975.
8. Hawk, J. Dennis; and Bristow, Dean R.: *Development of MCAERO Wing Design Panel Method With Interactive Graphics Module*. NASA CR-3775, 1984.
9. Beyer, William H., ed.: *CRC Standard Mathematical Tables*, 25th ed. CRC Press, Inc., 1978.
10. Hart, John F.; Cheney, E. W.; Lawson, Charles L.; Maehly, Hans J.; Mesztenyi, Charles K.; Rice, John R.; Thacher, Henry G., Jr.; and Witzgall, Christoph: *Computer Approximations*. John Wiley & Sons, Inc., c.1968, pp. 130-136.

TABLE I. TRANSITION-DUCT DIMENSIONS

(a) Configuration 1

$x/l$	$x$ , in.	$a$ , in.	$b$ , in.	AR	$A_{cs}$ , in <sup>2</sup>	$\eta$
0.0000	0.0000	2.5320	2.5320	1.0000	20.1408	2.0000
.0500	.2532	2.6877	2.4500	1.0970		1.8723
.1000	.5064	2.8434	2.3680	1.2008		1.7801
.1500	.7596	2.9991	2.2860	1.3120		1.7129
.2000	1.0128	3.1548	2.2040	1.4314		1.6647
.2500	1.2660	3.3105	2.1220	1.5601		1.6315
.3000	1.5192	3.4662	2.0399	1.6992		1.6112
.3500	1.7724	3.6220	1.9579	1.8499		1.6023
.4000	2.0256	3.7777	1.8759	2.0138		1.6044
.4500	2.2788	3.9334	1.7939	2.1926		1.6176
.5000	2.5320	4.0891	1.7119	2.3886		1.6427
.5500	2.7852	4.2448	1.6299	2.6043		1.6814
.6000	3.0384	4.4005	1.5479	2.8429		1.7364
.6500	3.2916	4.5562	1.4659	3.1082		1.8123
.7000	3.5448	4.7119	1.3839	3.4049		1.9167
.7500	3.7980	4.8676	1.3019	3.7390		2.0625
.8000	4.0512	5.0233	1.2198	4.1180		2.2741
.8500	4.3044	5.1790	1.1378	4.5517		2.6030
.9000	4.5576	5.3347	1.0558	5.0527		3.1853
.9500	4.8108	5.4904	.9738	5.6381		4.5682
1.0000	5.0640	5.6462	.8918	6.3312	50.0000	

(b) Configuration 2

$x/l$	$x$ , in.	$a$ , in.	$b$ , in.	AR	$A_{cs}$ , in <sup>2</sup>	$\eta$
0.0000	0.0000	2.5320	2.5320	1.0000	20.1408	2.0000
.0500	.2532	2.520	2.5201	1.0137		1.9787
.1000	.5064	2.6192	2.4861	1.0535		1.9233
.1500	.7596	2.7212	2.4324	1.1187		1.8499
.2000	1.0128	2.8559	2.3614	1.2094		1.7739
.2500	1.2660	3.0186	2.2757	1.3264		1.7060
.3000	1.5192	3.2046	2.1777	1.4716		1.6526
.3500	1.7724	3.4094	2.0699	1.6472		1.6172
.4000	2.0256	3.6282	1.9547	1.8562		1.6022
.4500	2.2788	3.8563	1.8345	2.1021		1.6097
.5000	2.5320	4.0891	1.7119	2.3886		1.6427
.5500	2.7852	4.3218	1.5893	2.7193		1.7063
.6000	3.0384	4.5499	1.4692	3.0970		1.8088
.6500	3.2916	4.7687	1.3539	3.5221		1.9642
.7000	3.5448	4.9735	1.2461	3.9912		2.1969
.7500	3.7980	5.1595	1.1481	4.4940		2.5522
.8000	4.0512	5.3222	1.0624	5.0096		3.1221
.8500	4.3044	5.4569	.9915	5.5039		4.1228
.9000	4.5576	5.5589	.9378	5.9279		6.2043
.9500	4.8108	5.6235	.9037	6.2226		12.6041
1.0000	5.0640	5.6461	.8918	6.3308	50.0000	

TABLE I. Continued

(c) Configuration 3

$x/l$	$x$ , in.	$a$ , in.	$b$ , in.	AR	$A_{cs}$ , in <sup>2</sup>	$\eta$
0.0000	0.0000	2.5320	2.5320	1.0000	20.1408	2.0000
.0500	.1899	2.5546	2.5201	1.0137	↓	1.9787
.1000	.3798	2.6192	2.4861	1.0535		1.9233
.1500	.5697	2.7212	2.4324	1.1187		1.8499
.2000	.7596	2.8559	2.3614	1.2094		1.7739
.2500	.9495	3.0186	2.2757	1.3264		1.7060
.3000	1.1394	3.2046	2.1777	1.4716		1.6526
.3500	1.3293	3.4094	2.0699	1.6472		1.6172
.4000	1.5192	3.6282	1.9546	1.8562		1.6022
.4500	1.7091	3.8563	1.8345	2.1021		1.6097
.5000	1.8990	4.0890	1.7119	2.3886		1.6428
.5500	2.0889	4.3218	1.5893	2.7193		1.7064
.6000	2.2788	4.5499	1.4691	3.0970		1.8089
.6500	2.4687	4.7687	1.3539	3.5221		1.1970
.7000	2.6586	4.9734	1.2460	3.9913		2.1970
.7500	2.8485	5.1595	1.1481	4.4941		2.5525
.8000	3.0384	5.3222	1.0624	5.0098		3.1227
.8500	3.2283	5.4569	.9914	5.5041		4.1244
.9000	3.4182	5.5589	.9377	5.9281		6.2102
.9500	3.6081	5.6235	.9037	6.2229		12.6555
1.0000	3.7980	5.6461	.8918	6.3312	50.0000	

(d) Configuration 4

$x/l$	$x$ , in.	$a$ , in.	$b$ , in.	AR	$A_{cs}$ , in <sup>2</sup>	$\eta$
0.0000	0.0000	2.5320	2.5320	1.0000	20.1408	2.0000
.0500	.1266	2.5546	2.5201	1.0137	↓	1.9787
.1000	.2532	2.6192	2.4861	1.0535		1.9233
.1500	.3798	2.7212	2.4324	1.1187		1.8499
.2000	.5064	2.8559	2.3614	1.2094		1.7739
.2500	.6330	3.0186	2.2757	1.3264		1.7060
.3000	.7596	3.2046	2.1777	1.4716		1.6526
.3500	.8862	3.4094	2.0699	1.6472		1.6172
.4000	1.0128	3.6282	1.9546	1.8562		1.6022
.4500	1.1394	3.8563	1.8345	2.1021		1.6097
.5000	1.2660	4.0890	1.7119	2.3886		1.6427
.5500	1.3926	4.3218	1.5893	2.7193		1.7064
.6000	1.5192	4.5499	1.4692	3.0970		1.8088
.6500	1.6458	4.7687	1.3539	3.5221		1.9642
.7000	1.7724	4.9735	1.1461	3.9913		2.1970
.7500	1.8990	5.1595	1.1481	4.4940		2.5524
.8000	2.0256	5.3222	1.0624	5.0097		3.1225
.8500	2.1522	5.4569	.9914	5.5040		4.1239
.9000	2.2788	5.5589	.9377	5.9281		6.2083
.9500	2.4054	5.6235	.9037	6.2228		12.6390
1.0000	2.5320	5.6461	.8918	6.3311	50.0000	

TABLE I. Concluded  
(e) Configuration 5

$x/l$	$x$ , in.	$a$ , in.	$b$ , in.	AR	$A_{cs}$ , in <sup>2</sup>	$\eta$
0.0000	0.0000	2.5320	2.5320	1.0000	20.1408	2.0000
.0500	.1917	2.5491	2.5192	1.0118	19.8891	1.9294
.1000	.3834	2.5980	1.4825	1.0464	19.6373	1.8521
.1500	.5751	2.6752	2.4251	1.1031	19.3855	1.7758
.2000	.7668	2.7772	2.3490	1.1823	19.1338	1.7072
.2500	.9585	2.9004	2.2570	1.2850	18.8820	1.6507
.3000	1.1502	3.0413	2.1519	1.4133	18.6303	1.6094
.3500	1.3419	3.1963	2.0362	1.5697	18.3785	1.5852
.4000	1.5336	3.3619	1.9126	1.7578	18.1267	1.5803
.4500	1.7253	3.5346	1.7837	1.9816	17.8750	1.5971
.5000	1.9170	3.7109	1.6522	2.2461	17.6232	1.6397
.5500	2.1087	3.8871	1.5206	2.5562	17.3715	1.7144
.6000	2.3004	4.0598	1.3917	2.9171	17.1197	1.8319
.6500	2.4921	4.2254	1.2681	3.3321	16.8679	2.0106
.7000	2.6938	4.3804	1.1524	3.8011	16.6162	2.2844
.7500	2.8755	4.5312	1.0473	4.3172	16.3644	2.7204
.8000	3.0672	4.6445	.9553	4.8617	16.1127	3.4741
.8500	3.2589	4.7465	.8792	5.3985	15.8609	5.0010
.9000	3.4506	4.8237	.8216	5.8712	15.6091	9.6171
.9500	3.6423	4.8726	.7851	6.2065	15.3574	50.0000
1.0000	3.8340	4.8897	.7723	6.3312	15.1056	50.0000

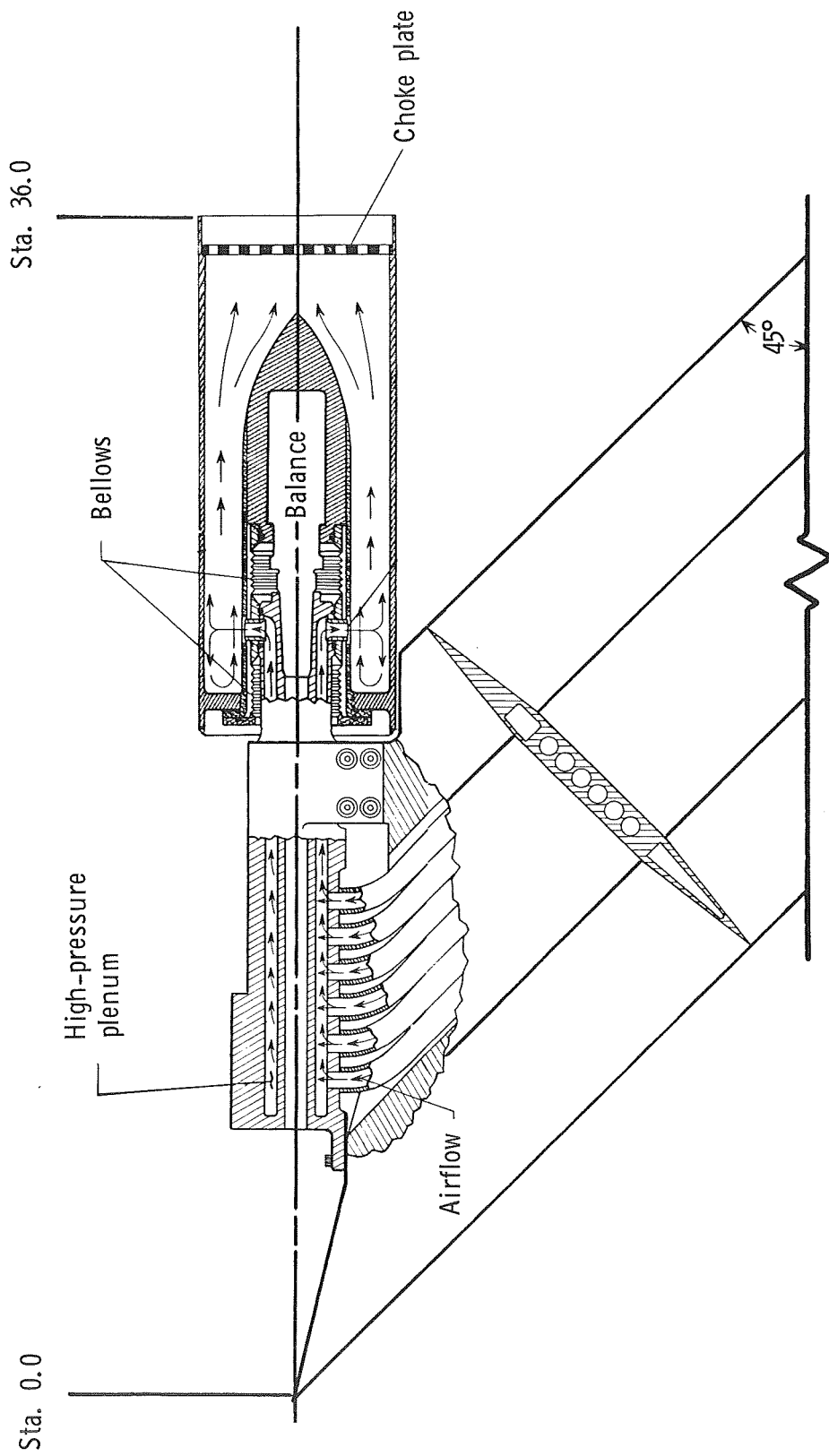


Figure 1. Model support and high-pressure air transfer system.

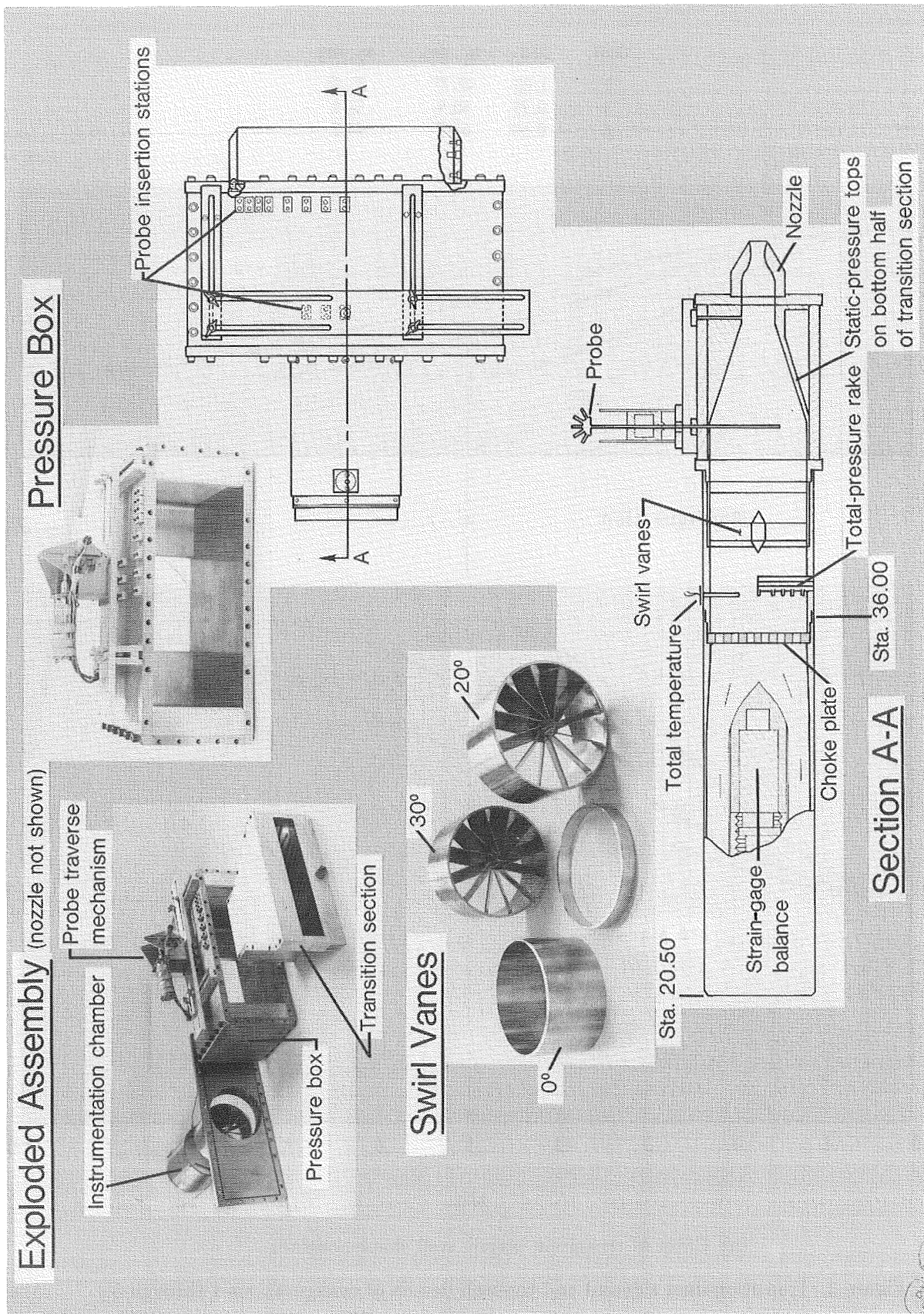
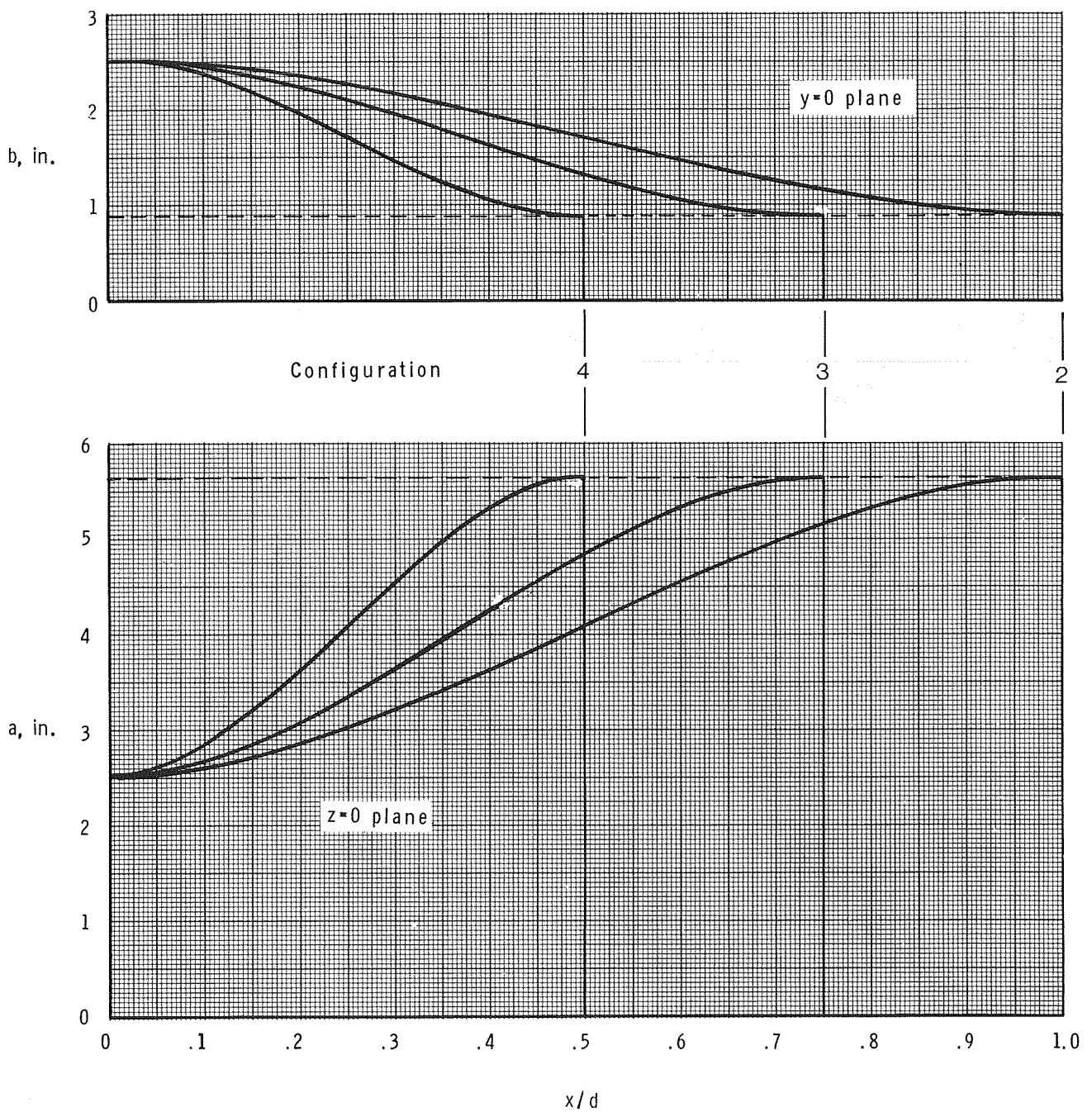


Figure 2. Drawing of test-rig assembly showing all components of model. All linear dimensions are in inches.

CONFIDENTIAL

Conf.	$l/d$	$\alpha_1$ , deg	$\alpha_2$ , deg
2	1.00	42.7°	25.9°
3	0.75	50.9	32.9
4	0.50	61.5	44.2

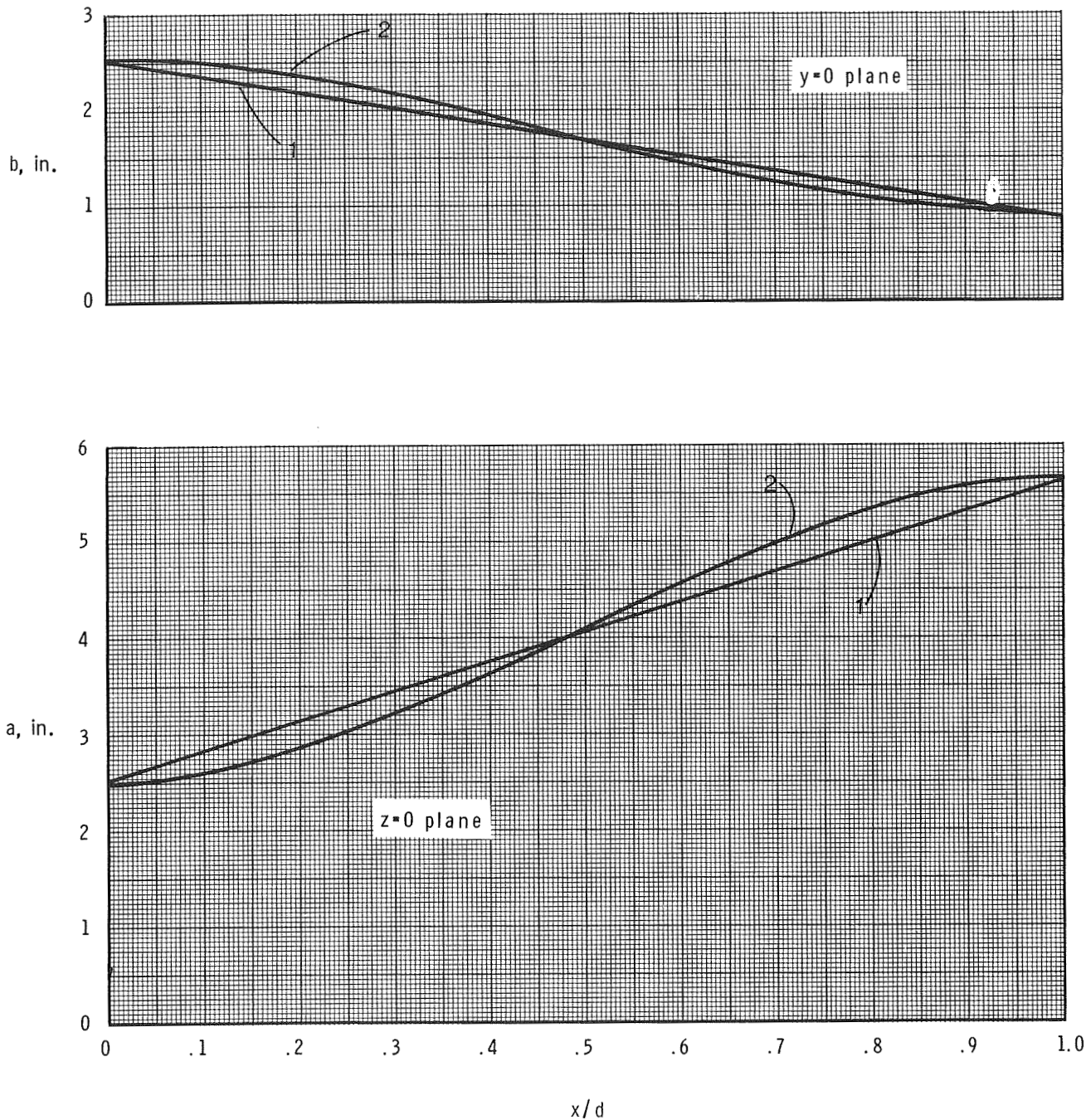


(a) Effect of transition length, wall shape constant.

Figure 3. Transition-duct sidewall and top-wall details of configurations 1 through 5.

ORIGINAL PAGE IS  
OF POOR QUALITY

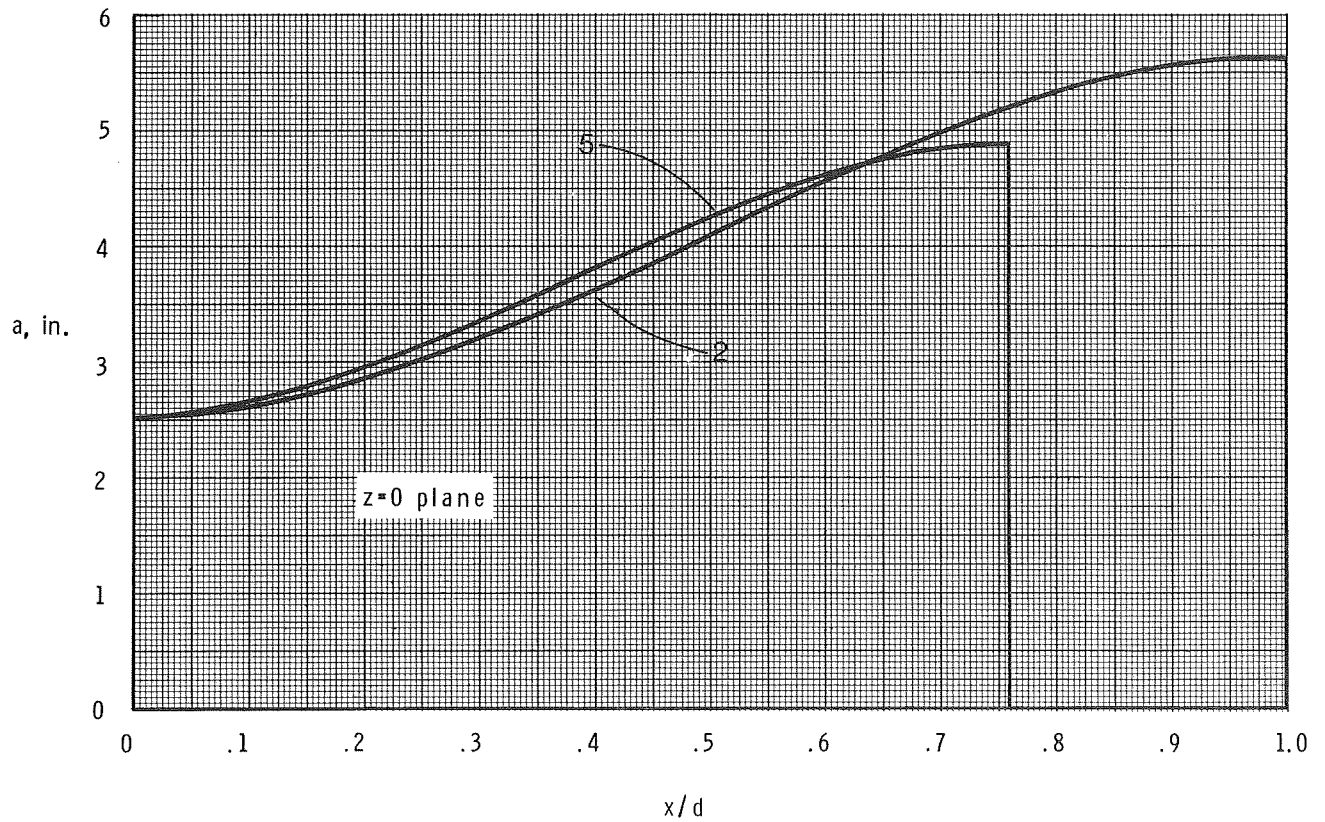
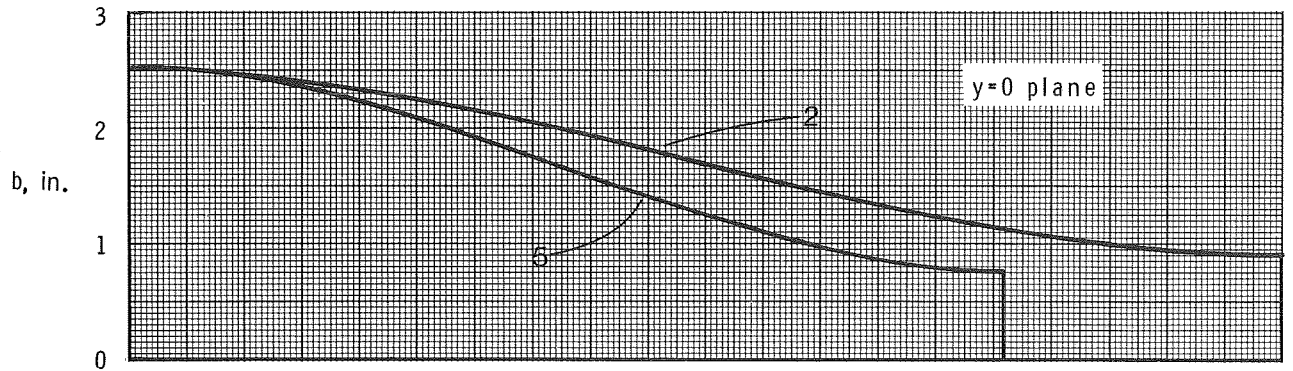
Conf.	$l/d$	$\alpha_1$ , deg	$\alpha_2$ , deg
1	1.00	31.6°	17.9°
2	1.00	42.7	25.9



(b) Effect of wall shape, length constant.

Figure 3. Continued.

Conf.	$l/d$	$\alpha_1$ , deg	$\alpha_2$ , deg
2	1.00	42.7°	25.9°
5	0.75	42.7	34.5



(c) Effect of area distribution, wall shape constant.

Figure 3. Concluded.

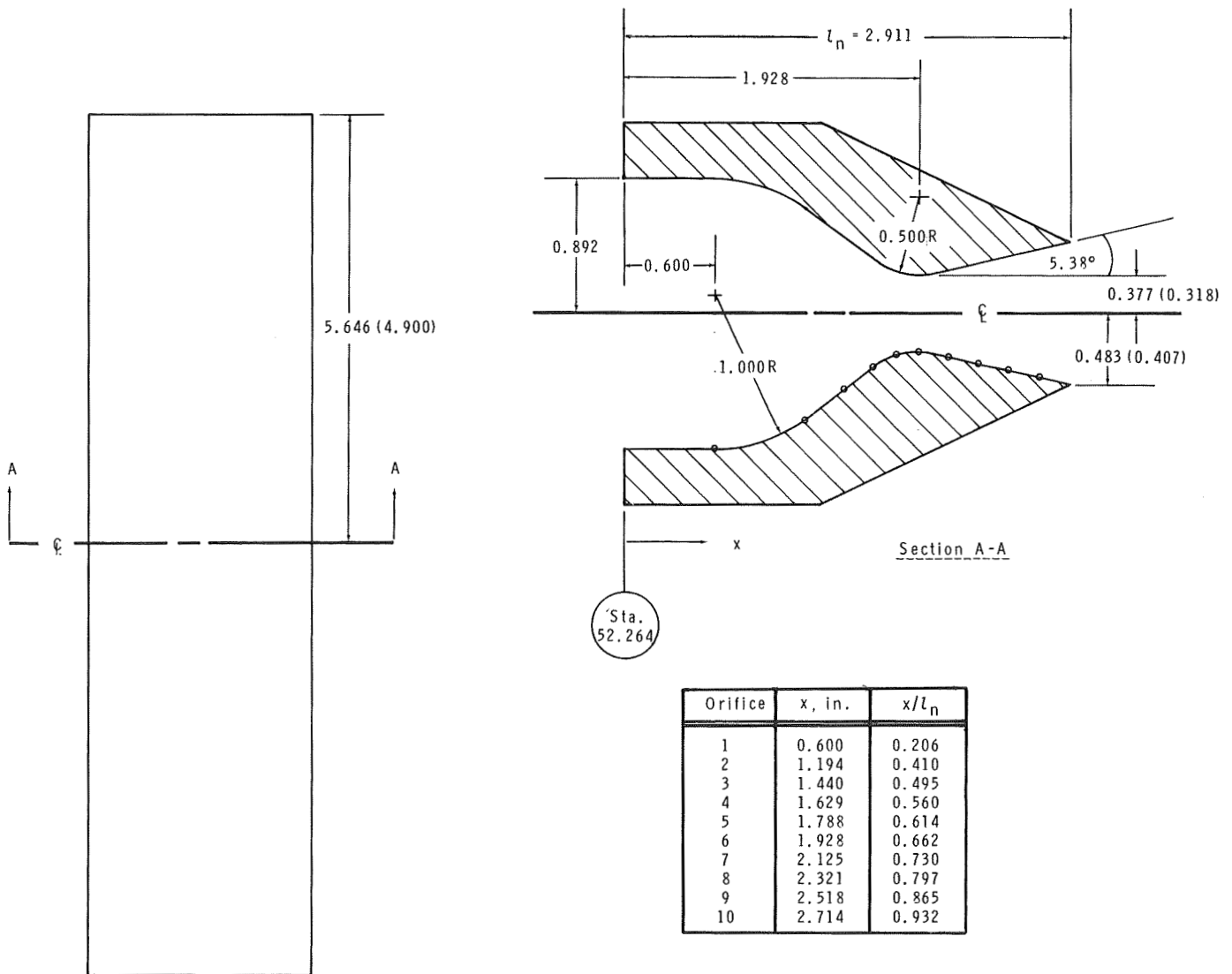
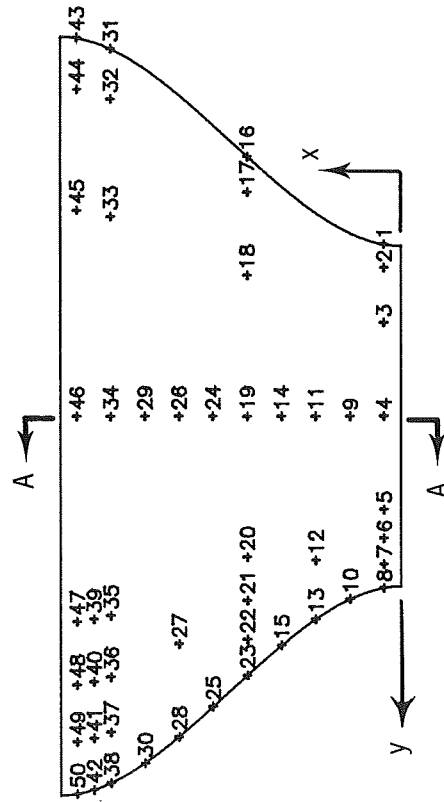
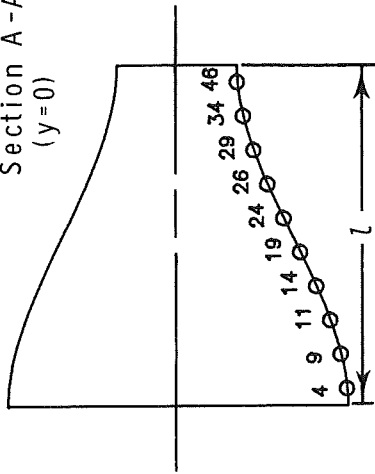


Figure 4. High-aspect-ratio dry-power nozzle geometry used with all transitions. Values in parentheses are for nozzle used with configuration 5 only. All linear dimensions are in inches.

Section A-A  
(y = 0)



Orifice	x/t	y/a	Orifice	x/t	y/a
1	.050	-1.000	26	.650	0.000
2	.050	-.862	27	.650	.711
3	.050	-.543	28	.650	1.000
4	.050	0.000	29	.750	0.000
5	.050	.543	30	.750	1.000
6	.050	.711	31	.850	-1.000
7	.050	.862	32	.850	-.863
8	.050	1.000	33	.850	-.543
9	.150	0.000	34	.850	0.000
10	.150	1.000	35	.850	.543
11	.250	0.000	36	.850	.711
12	.250	.711	37	.850	.863
13	.250	1.000	38	.850	1.000
14	.350	0.000	39	.900	.543
15	.350	1.000	40	.900	.711
16	.450	-1.000	41	.900	.863
17	.450	-.862	42	.900	1.000
18	.450	-.543	43	.950	-1.000
19	.450	0.000	44	.950	-.863
20	.450	.543	45	.950	-.544
21	.450	.711	46	.950	0.000
22	.450	.862	47	.950	.544
23	.450	1.000	48	.950	.712
24	.550	0.000	49	.950	.863
25	.550	1.000	50	.950	1.000

NOTE - The z coordinate of each orifice can be calculated from  

$$z = b \left\{ \left[ 1 - (y/a)^\eta \right]^{1/\eta} \right\}$$
 where a, b, and  $\eta$  are all functions of x.

Figure 5. Static-pressure-orifice locations (only on bottom half of each duct) for all transitions.

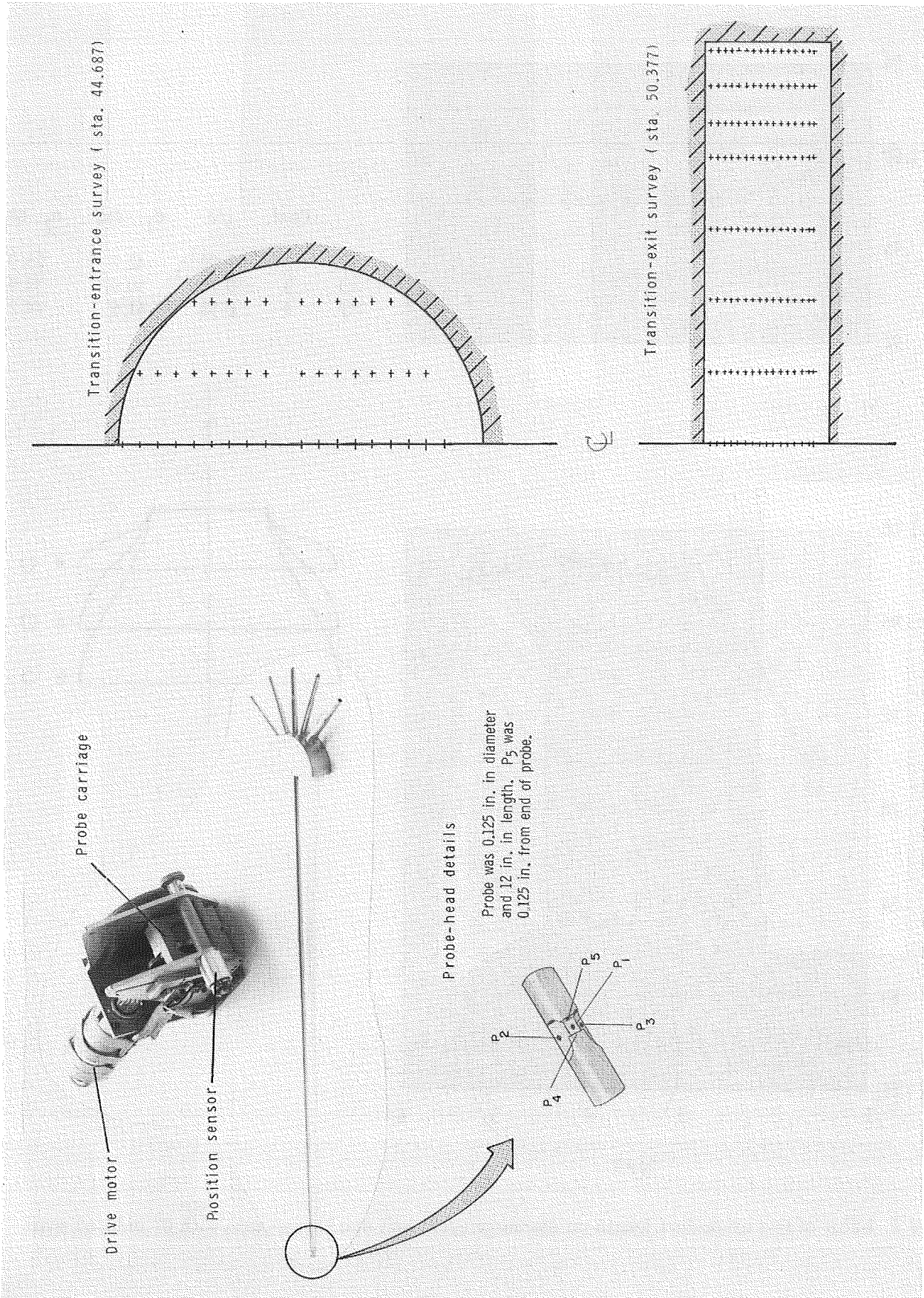
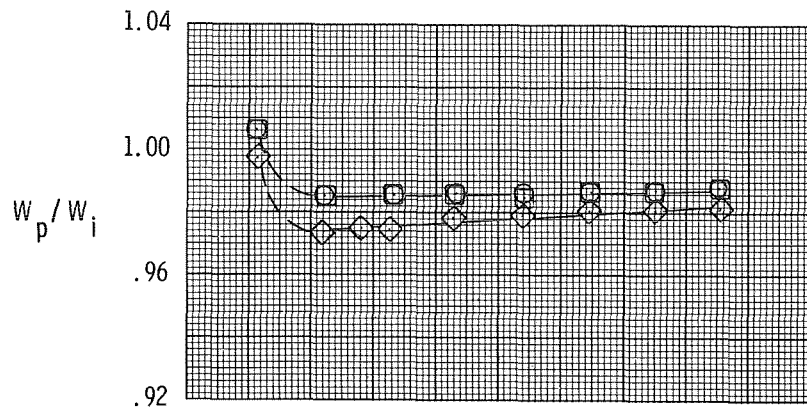


Figure 6. Pressure probe and survey location details for configuration 2.



Conf.	$l/d$	$\alpha_1$ , deg	$\alpha_2$ , deg	
○	2	1.00	42.7	25.9
□	3	0.75	50.9	32.9
◇	4	0.50	61.5	44.2

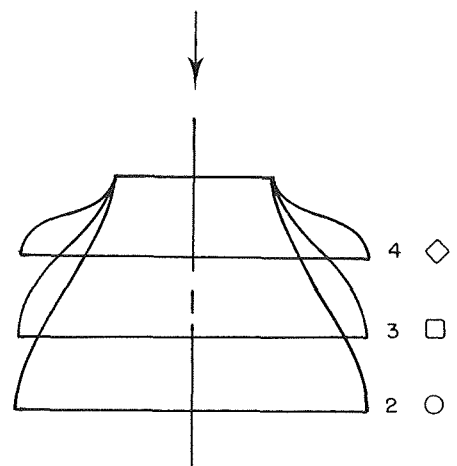
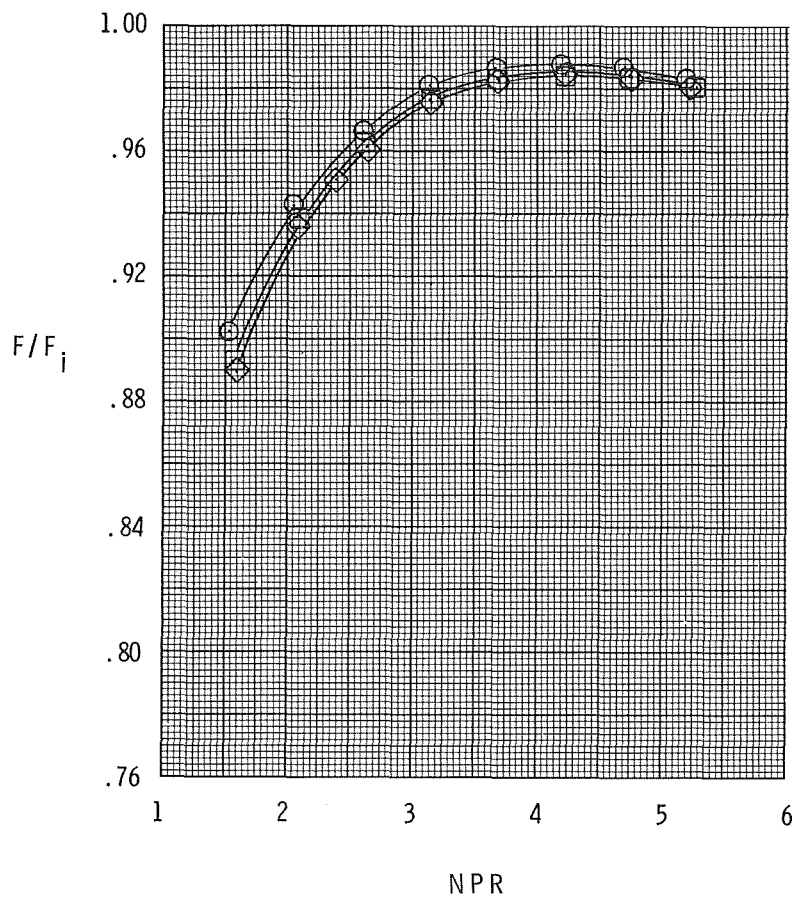
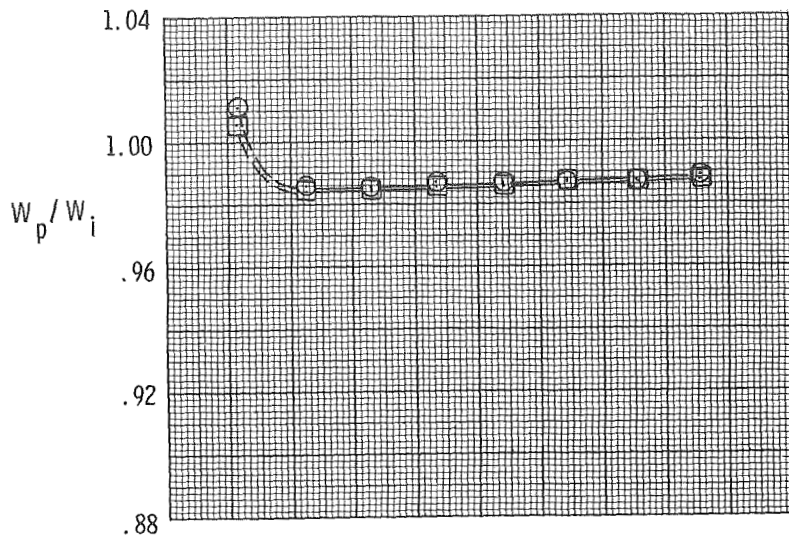


Figure 7. Effect of transition-duct length on discharge coefficient and thrust ratio with  $0^\circ$  induced swirl.



Conf.	$l/d$
□	1 1.00
○	2 1.00

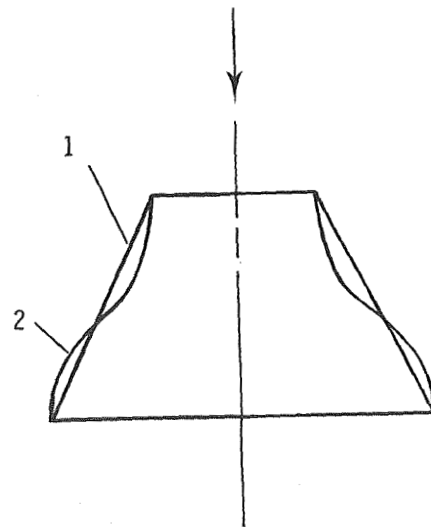
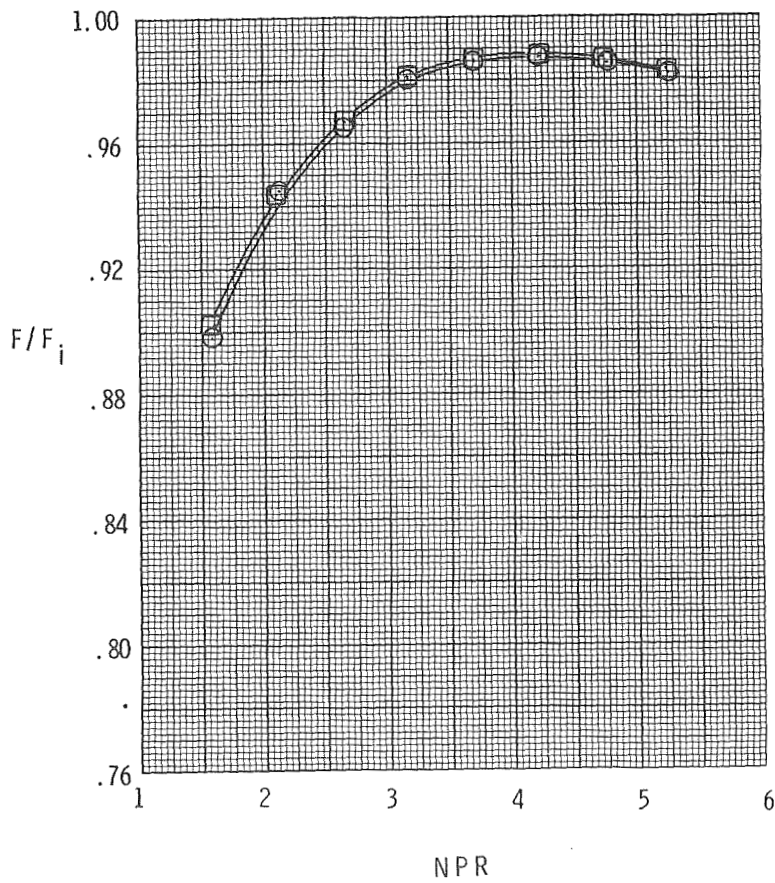
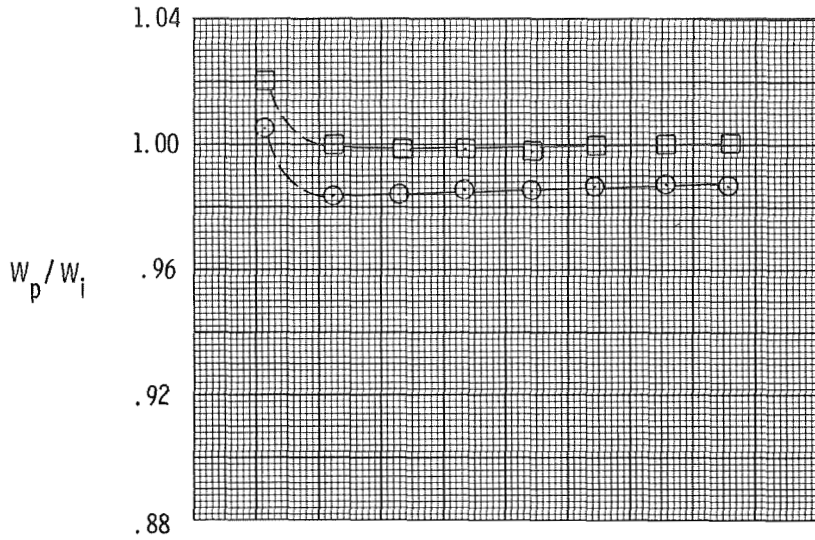


Figure 8. Effect of transition-duct sidewall shape on discharge coefficient and thrust ratio with  $0^\circ$  induced swirl.



Conf	$l/d$	$\alpha_1$ , deg	$\alpha_2$ , deg
○	2	42.7	25.9
□	5	42.7	34.5

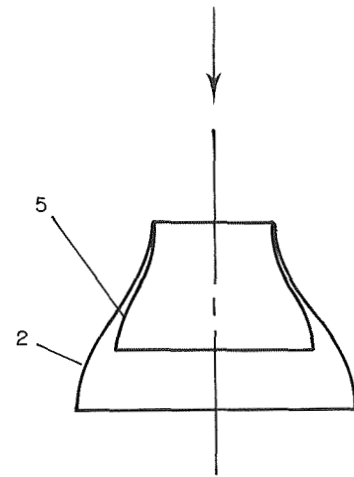
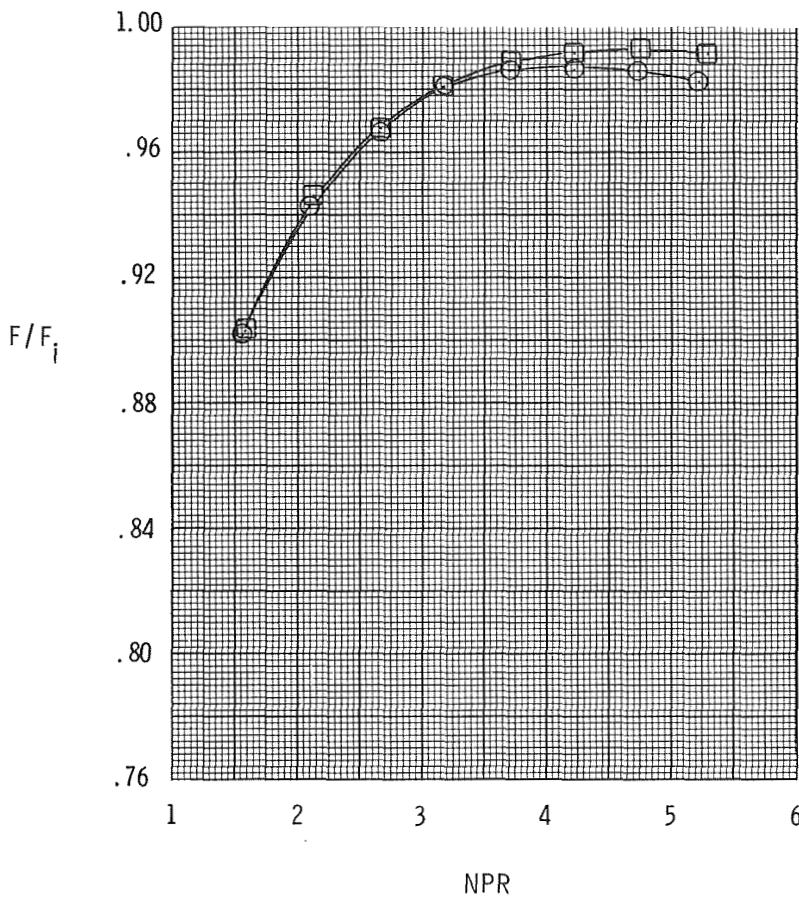


Figure 9. Effect of transition-duct area distribution on discharge coefficient and thrust ratio with  $0^\circ$  induced swirl.

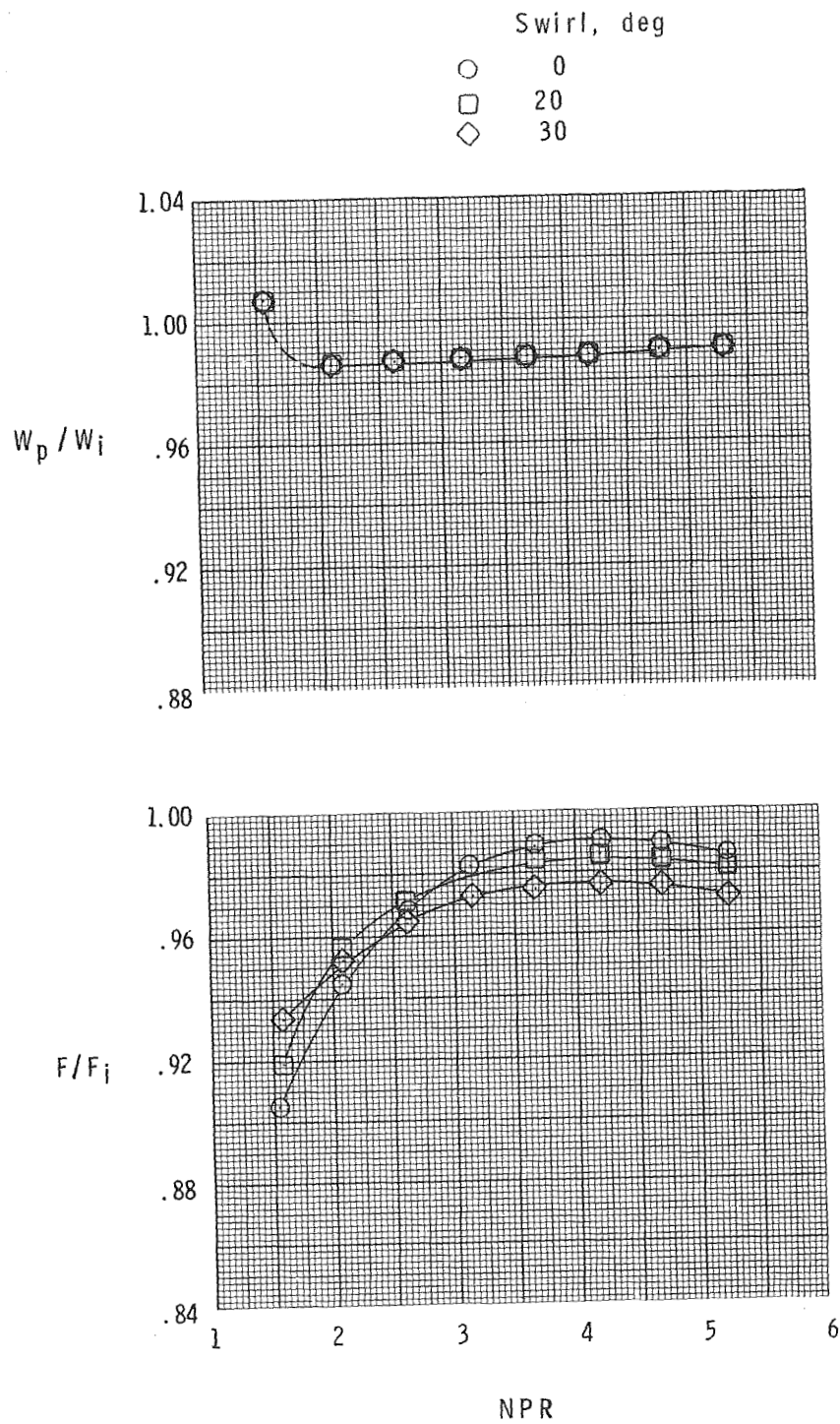
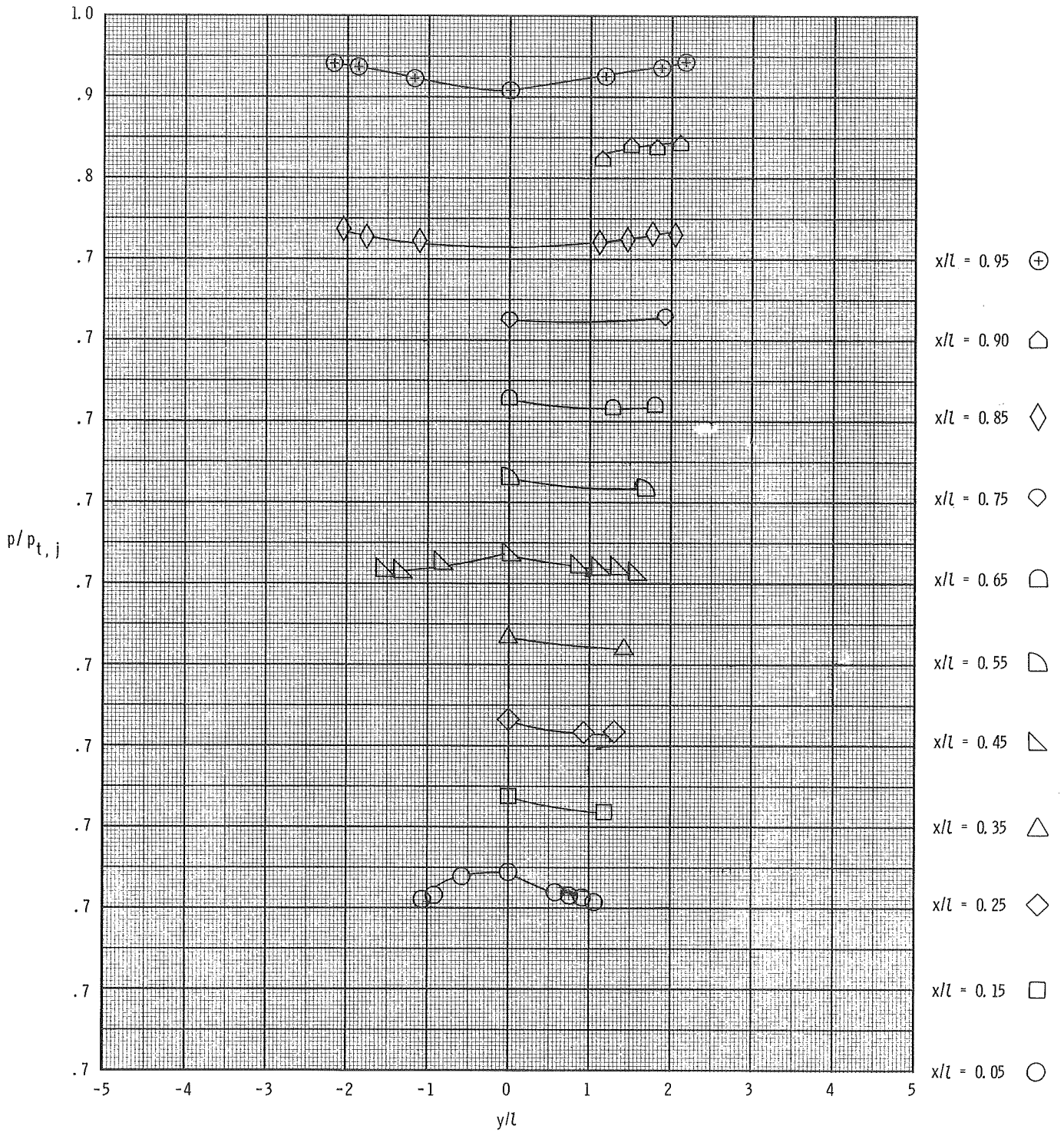


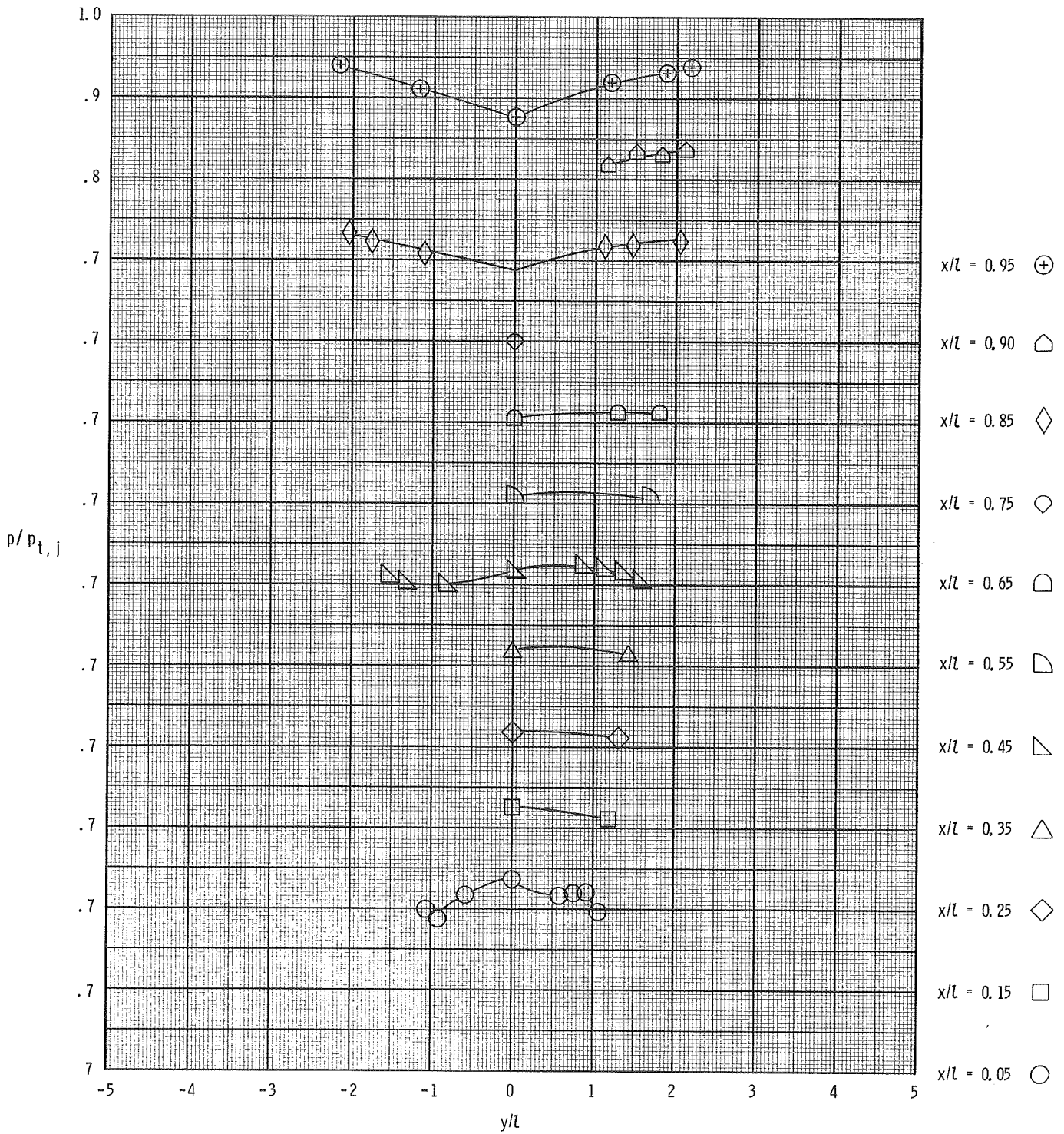
Figure 10. Effect of induced swirl on discharge coefficient and thrust ratio for transition-duct configuration 2.



(a) Configuration 1;  $0^\circ$  swirl; NPR = 3.17.

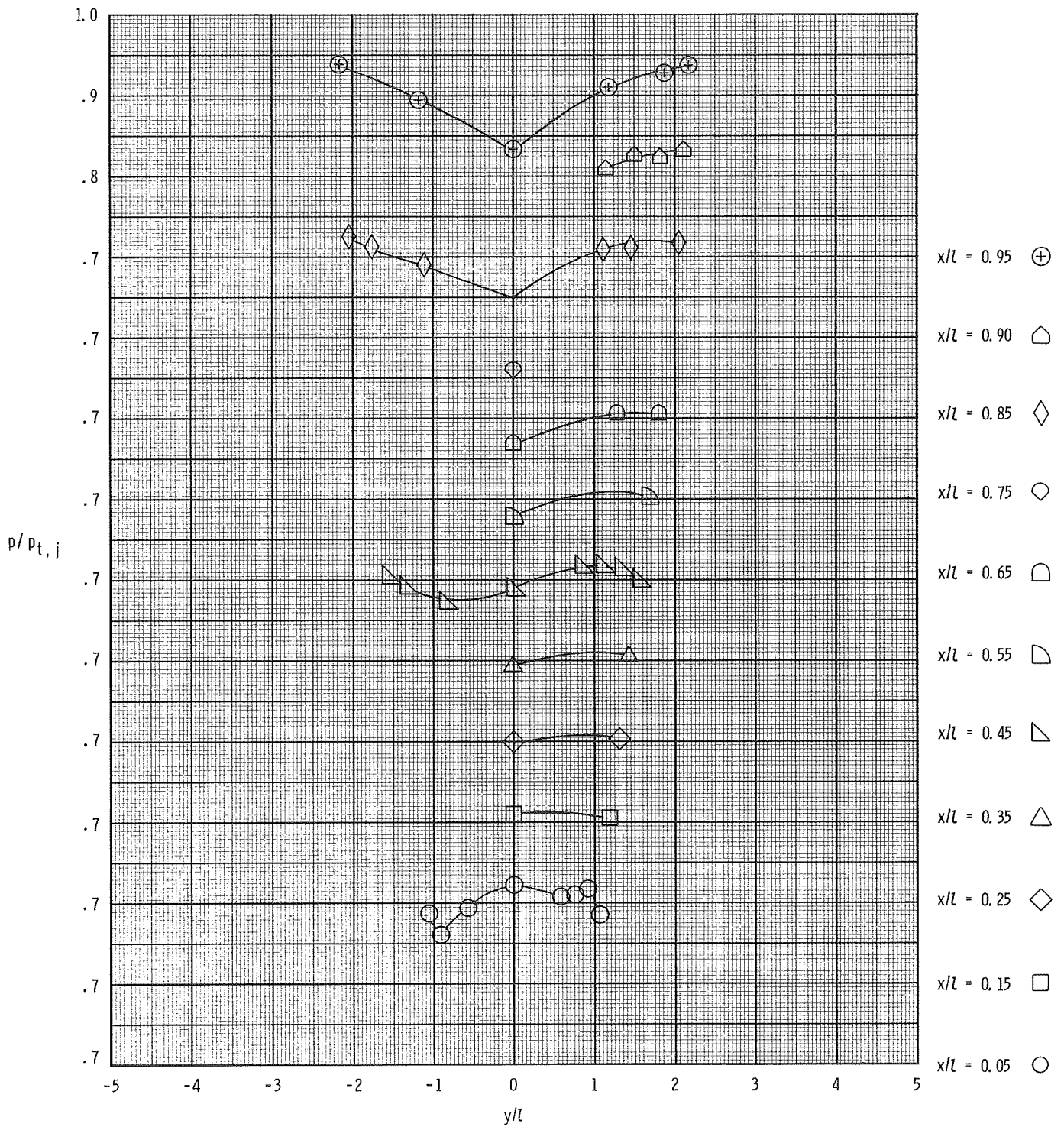
Figure 11. Variation of static-pressure ratio with position in the transition ducts for all configurations and swirl angles.

ORIGINAL PAGE IS  
OF POOR QUALITY



(b) Configuration 1; 20° swirl; NPR = 3.18.

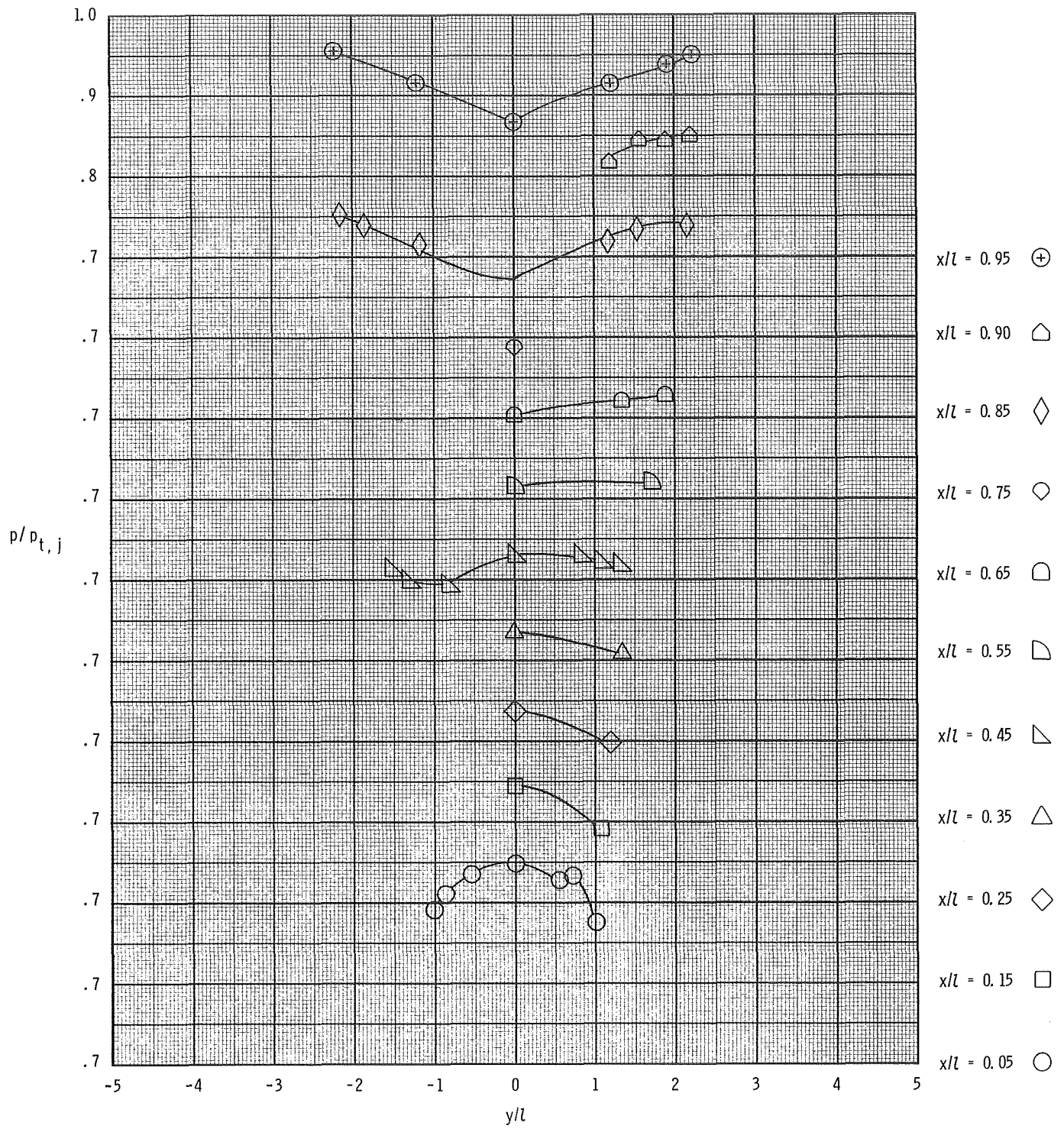
Figure 11. Continued.



(c) Configuration 1; 30° swirl; NPR = 3.18.

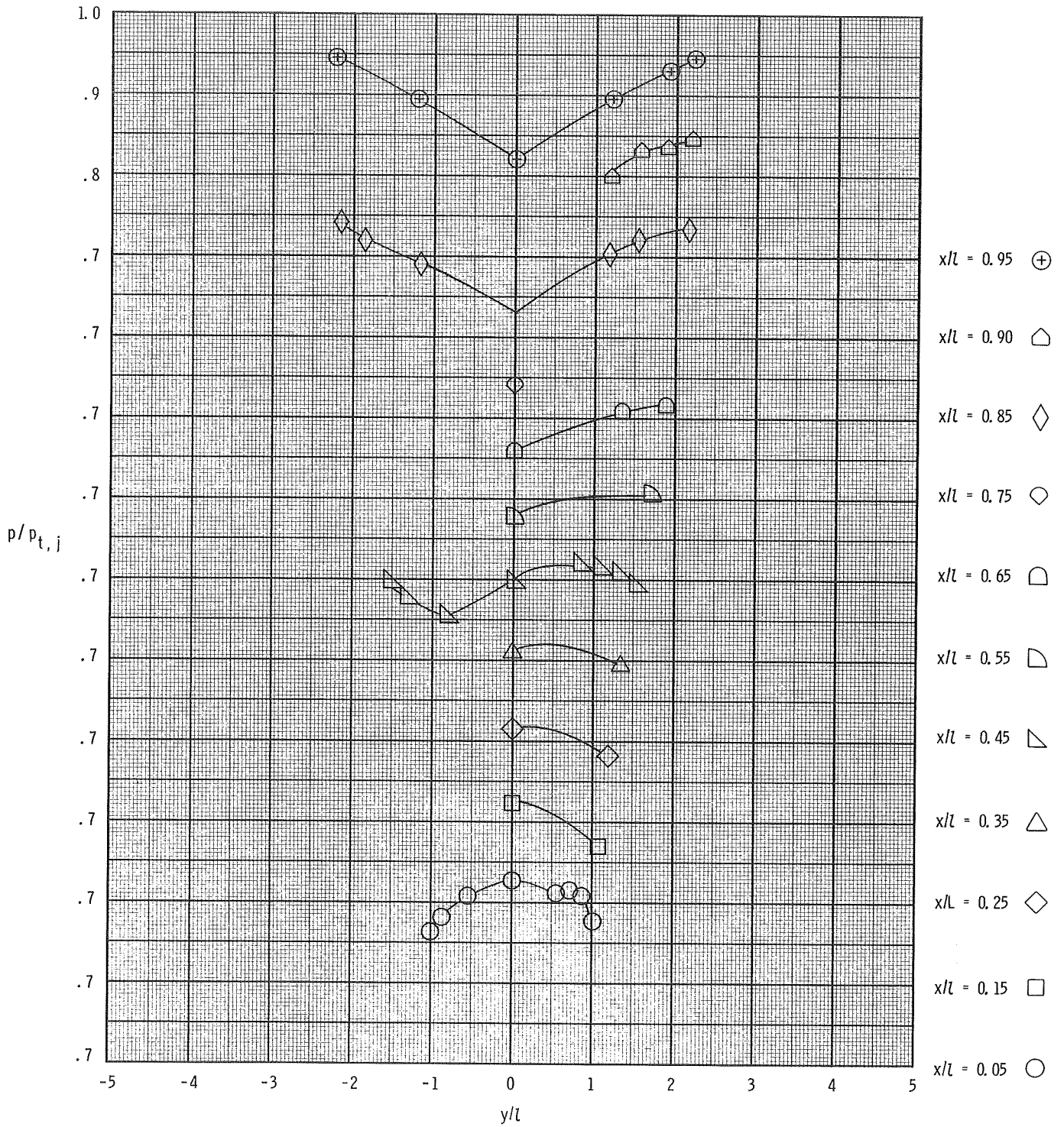
Figure 11. Continued.





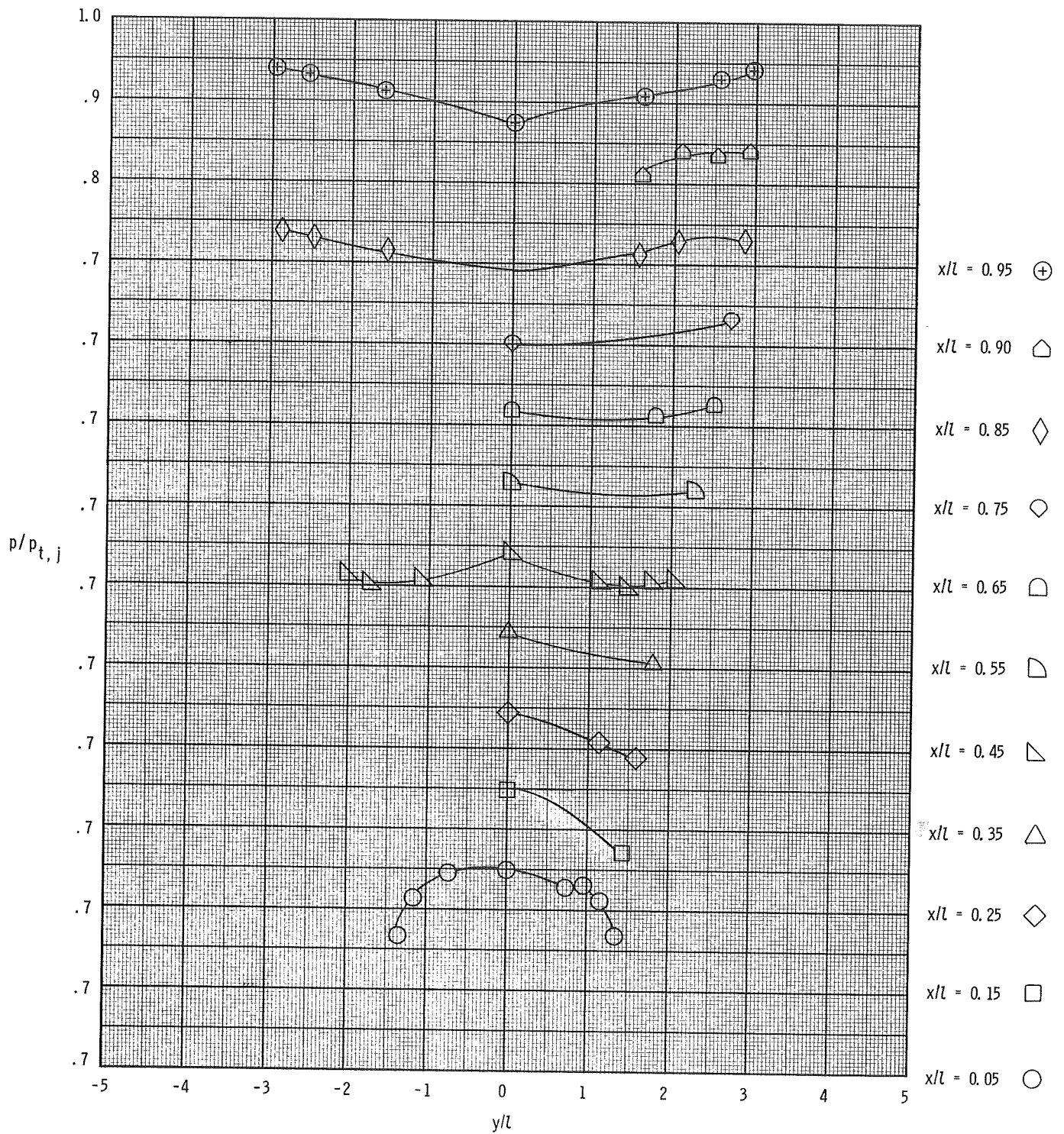
(e) Configuration 2; 20° swirl; NPR = 3.18.

Figure 11. Continued.



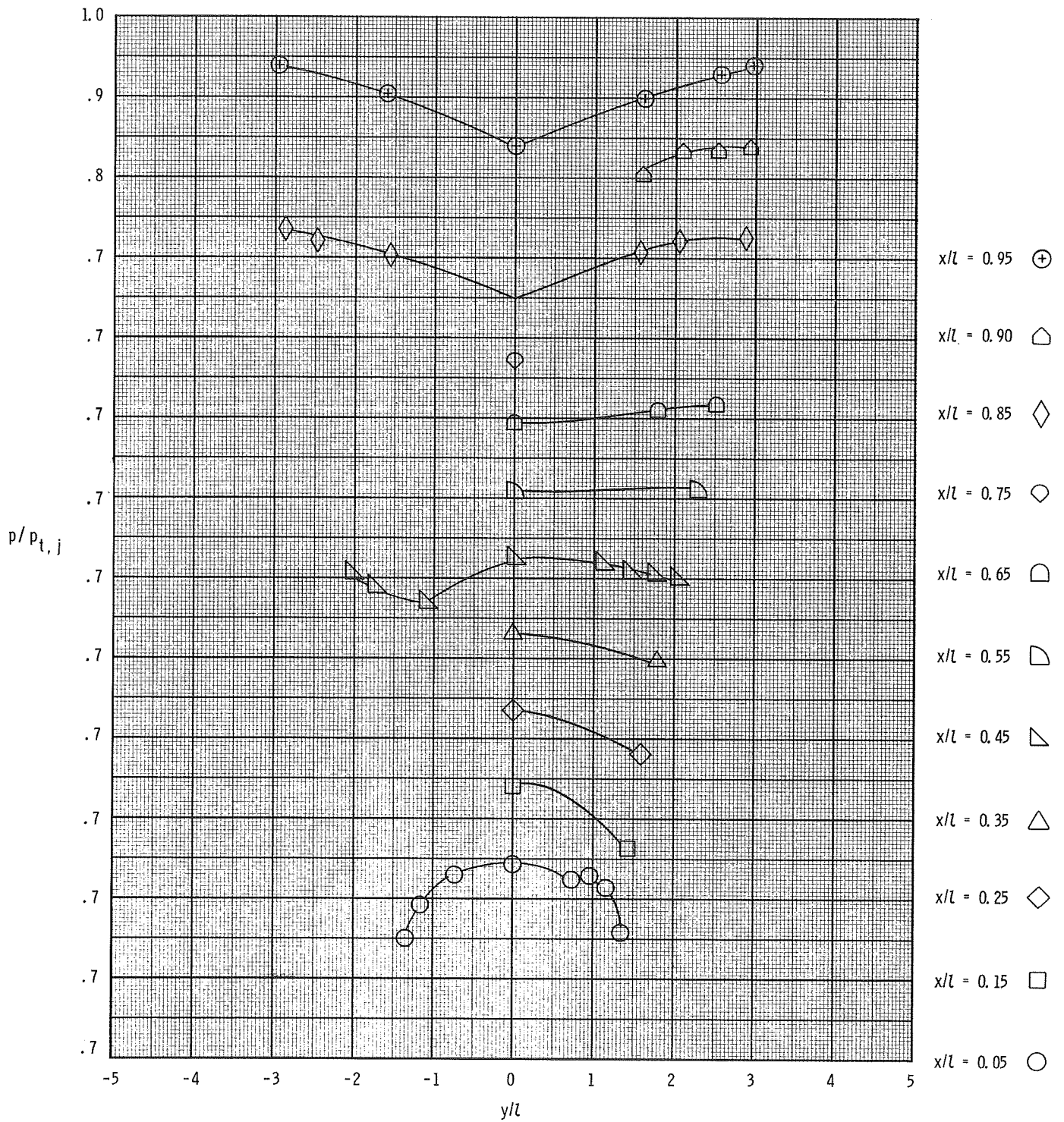
(f) Configuration 2; 30° swirl; NPR = 3.16.

Figure 11. Continued.



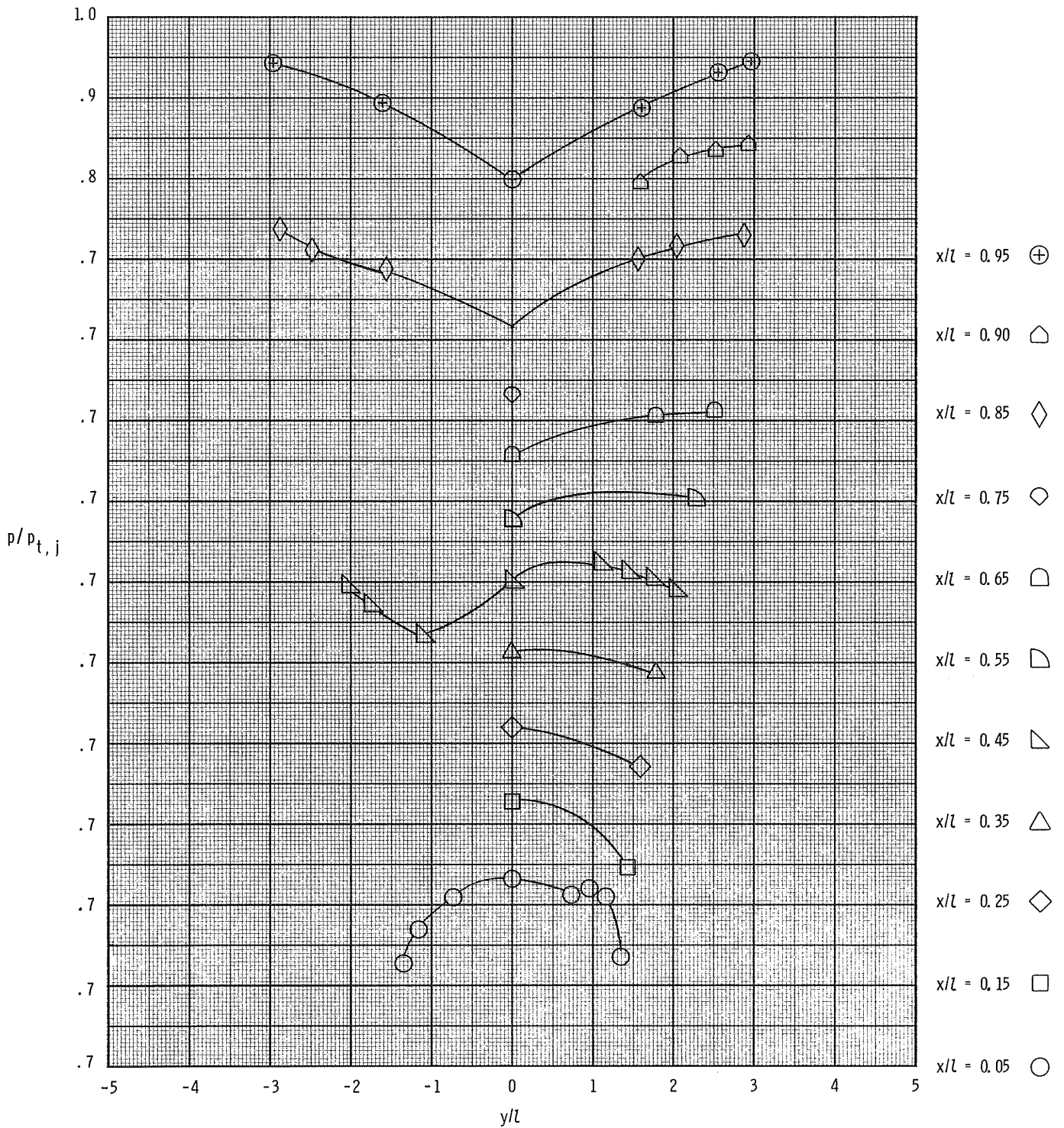
(g) Configuration 3;  $0^\circ$  swirl; NPR = 3.18.

Figure 11. Continued.



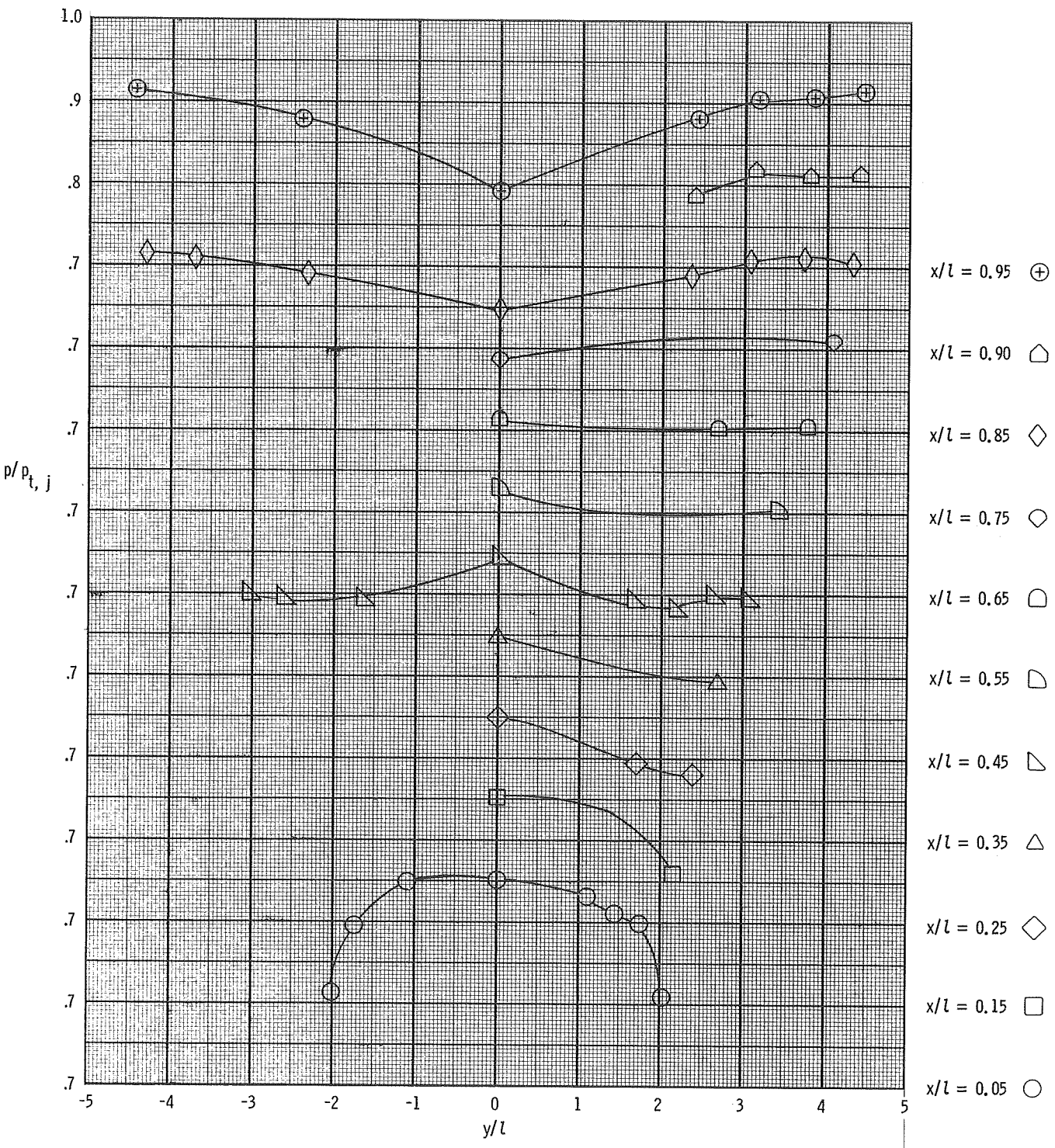
(h) Configuration 3; 20° swirl; NPR = 3.16.

Figure 11. Continued.



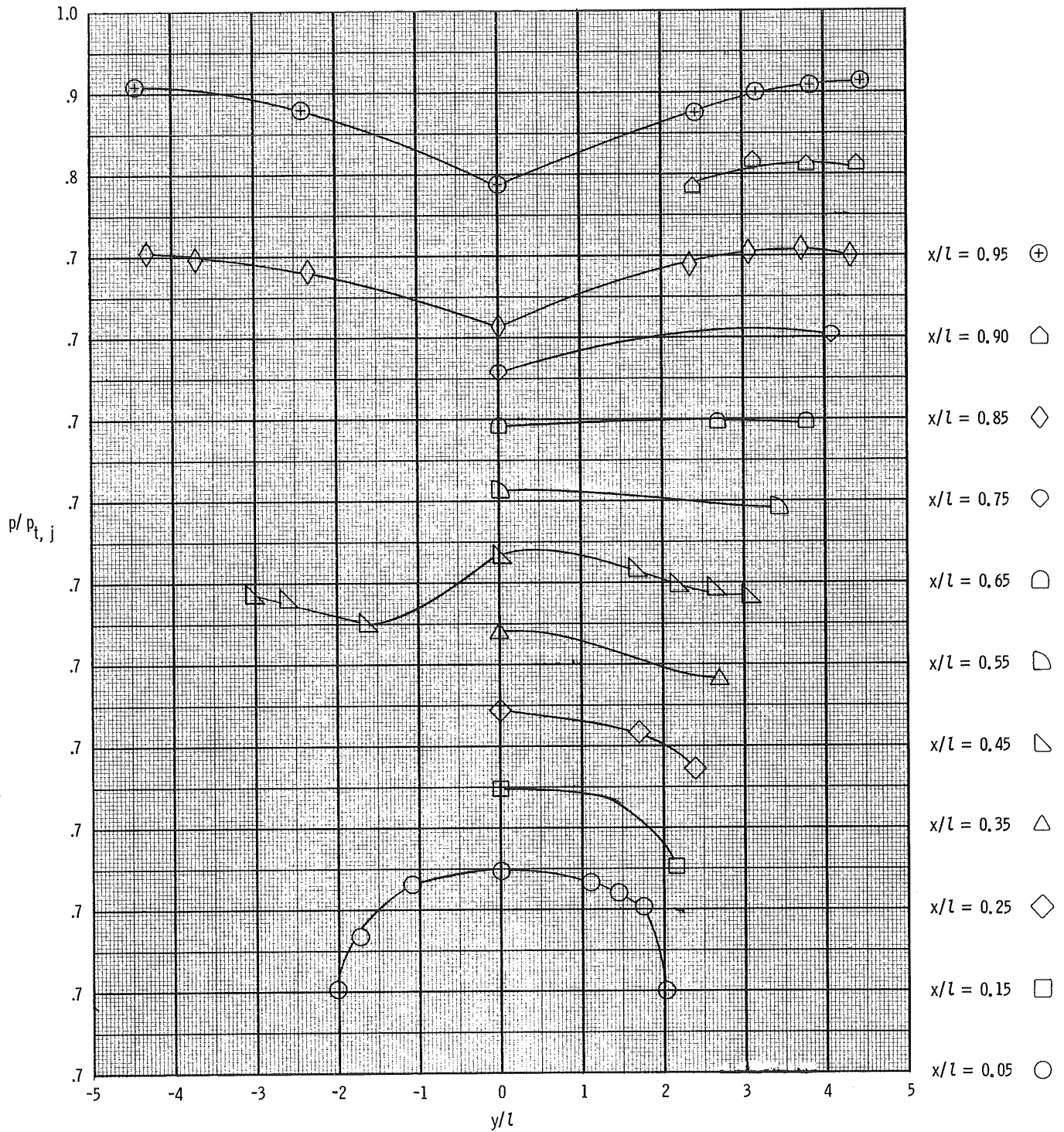
(i) Configuration 3; 30° swirl; NPR = 3.17.

Figure 11. Continued.



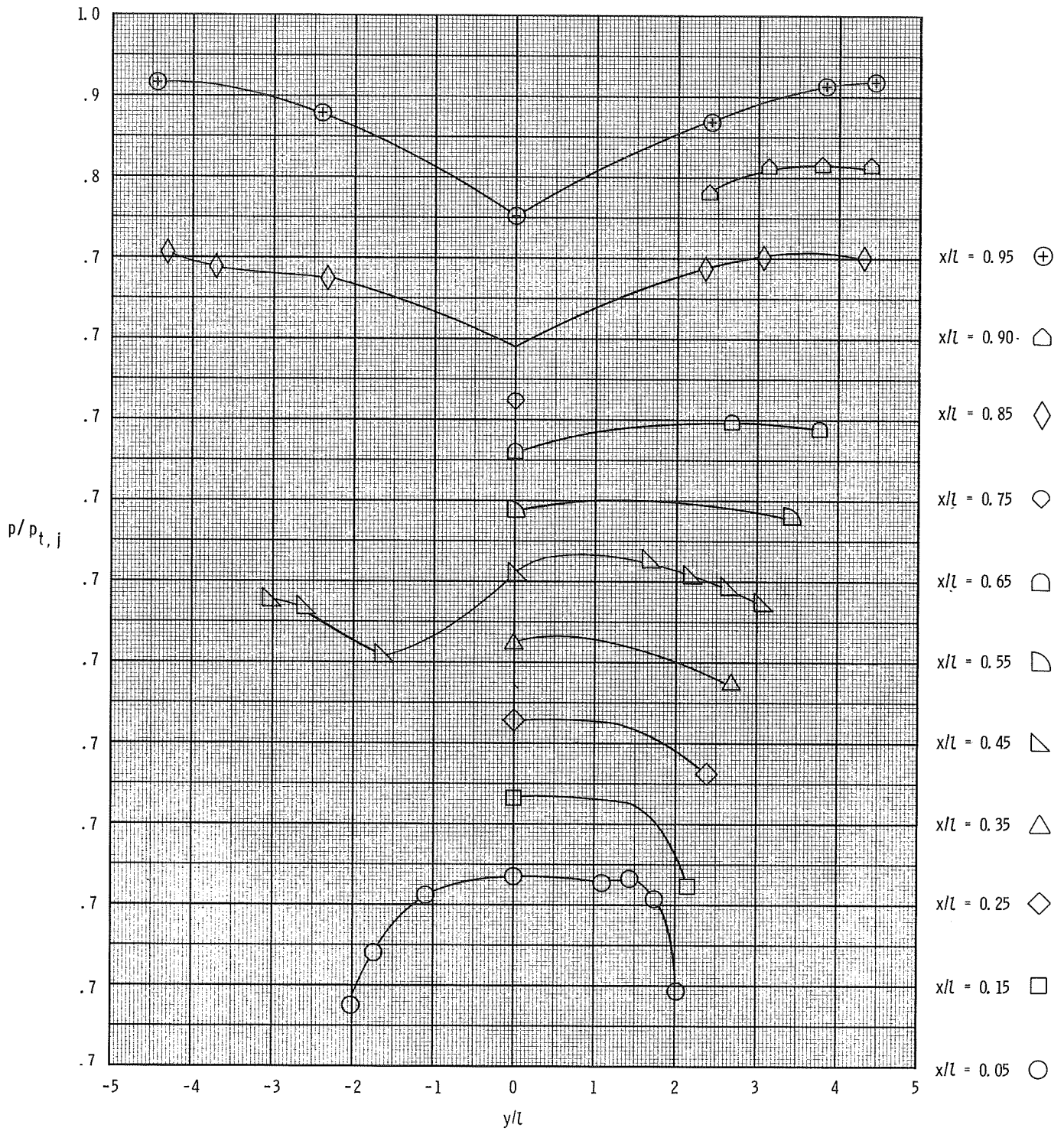
(j) Configuration 4;  $0^\circ$  swirl; NPR = 3.16.

Figure 11. Continued.



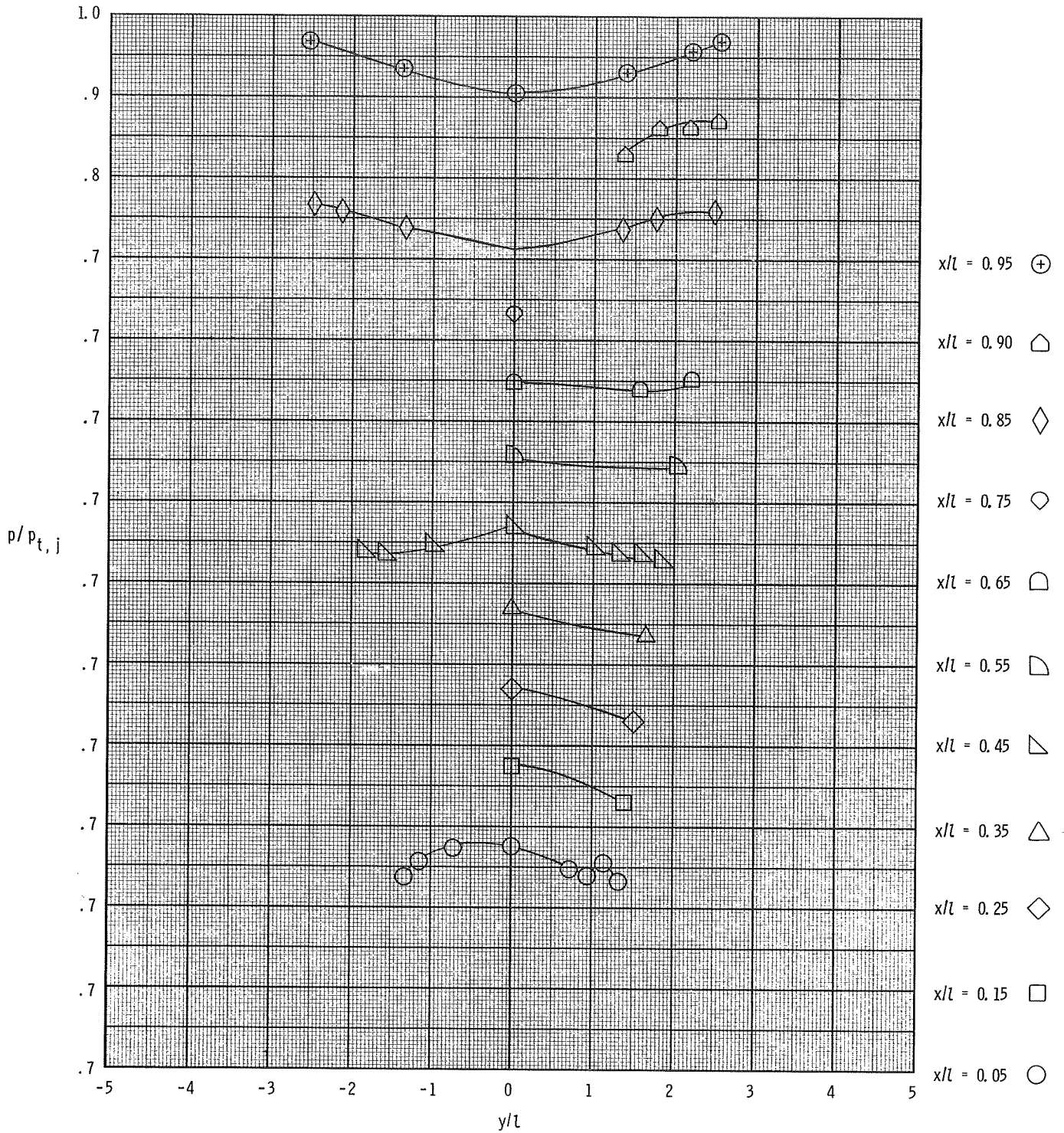
(k) Configuration 4; 20° swirl; NPR = 3.19.

Figure 11. Continued.



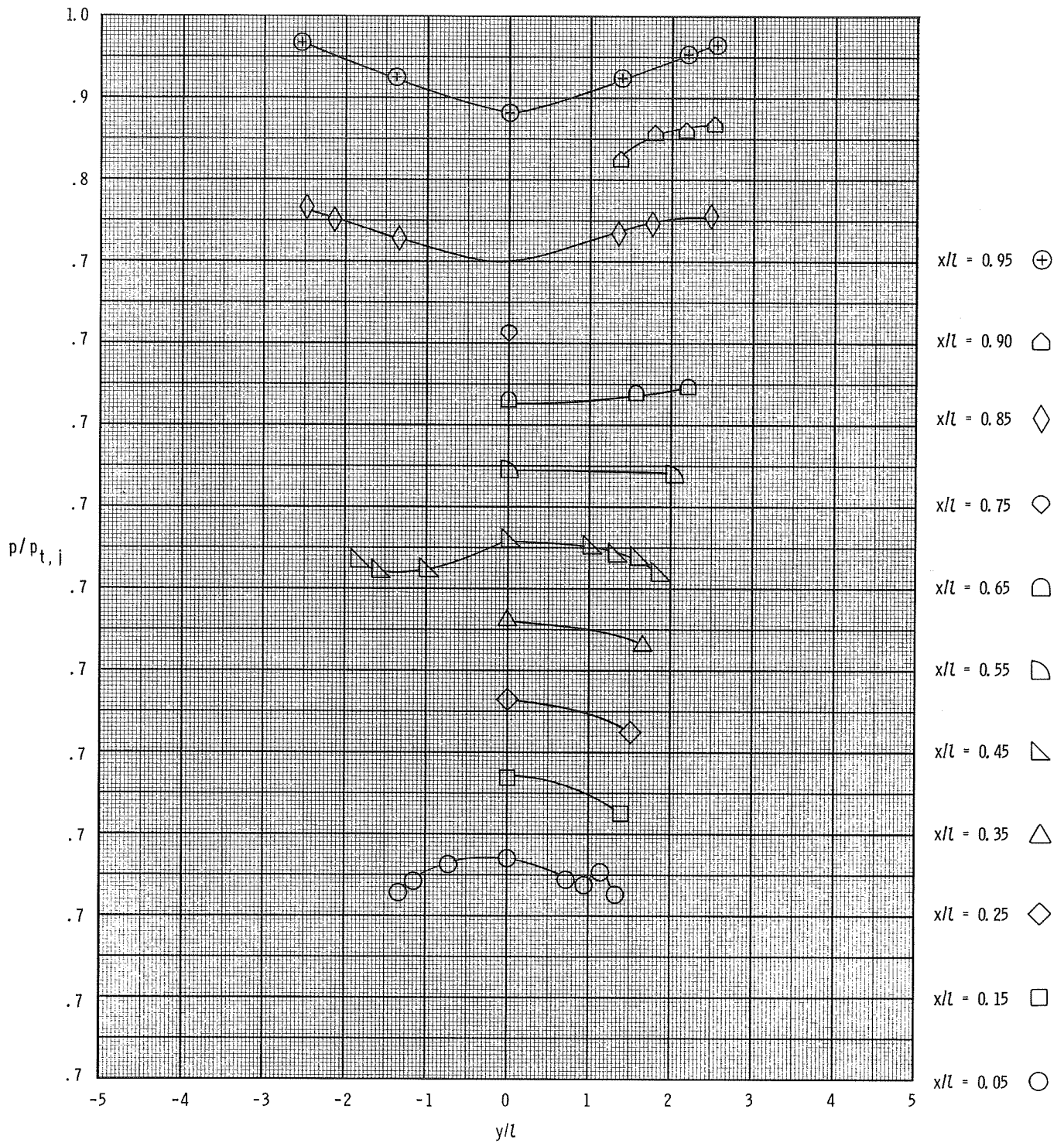
(l) Configuration 4; 30° swirl; NPR = 3.17.

Figure 11. Continued.



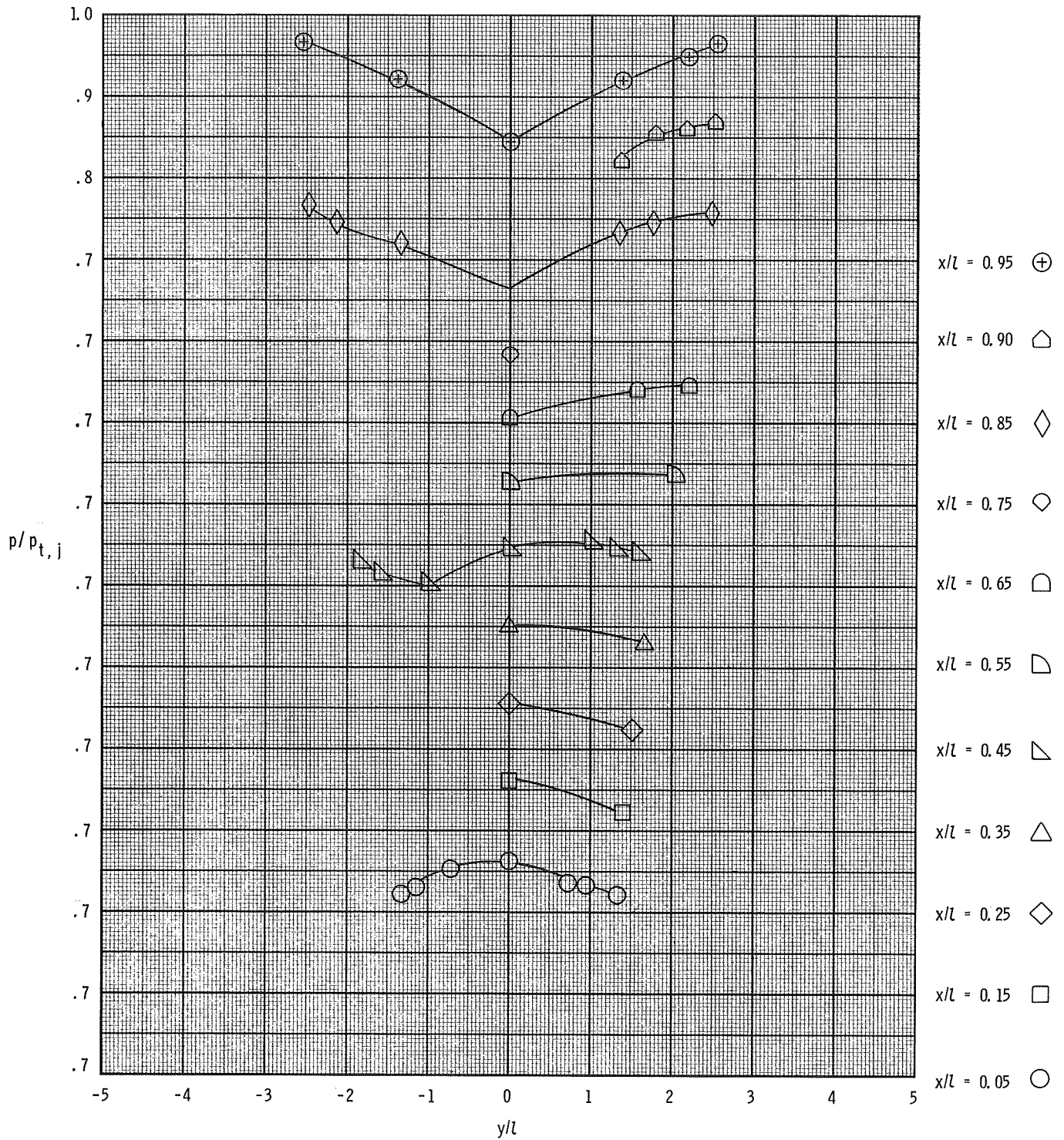
(m) Configuration 5;  $0^\circ$  swirl; NPR = 3.18.

Figure 11. Continued.



(n) Configuration 5; 20° swirl; NPR = 3.18.

Figure 11. Continued.



(o) Configuration 5; 30° swirl; NPR = 3.18.

Figure 11. Concluded.

NPR  
 ○ 1.27  
 □ 2.39  
 ◇ 4.24

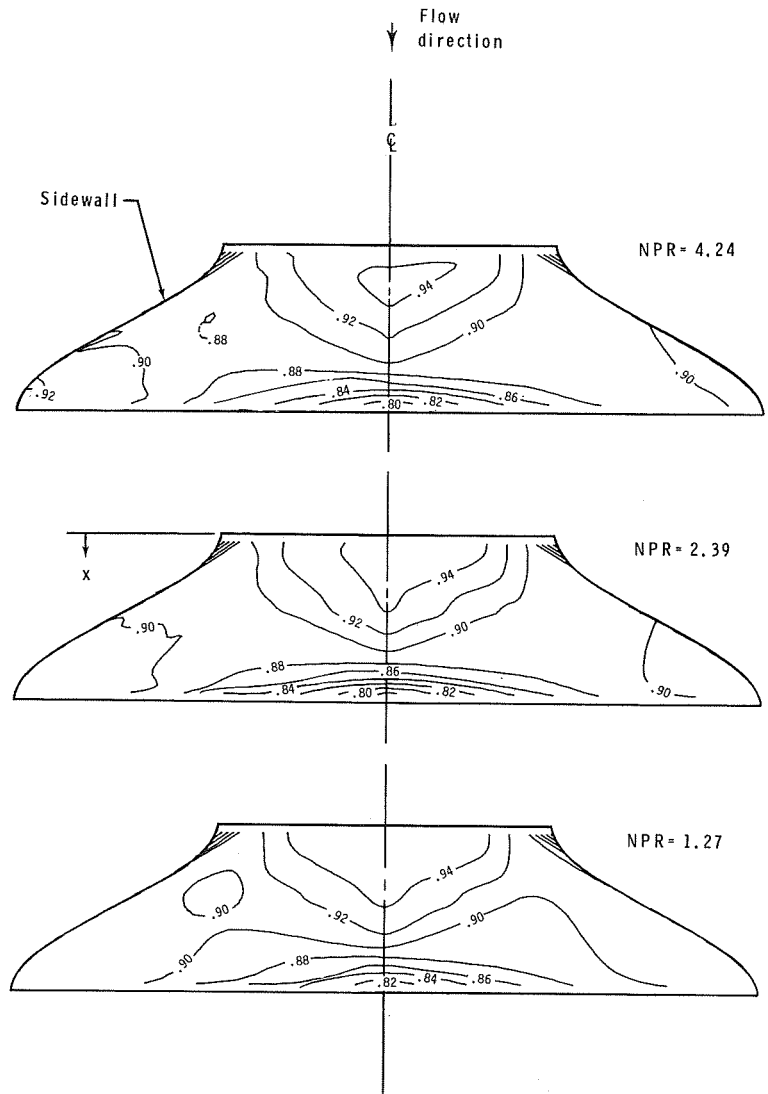
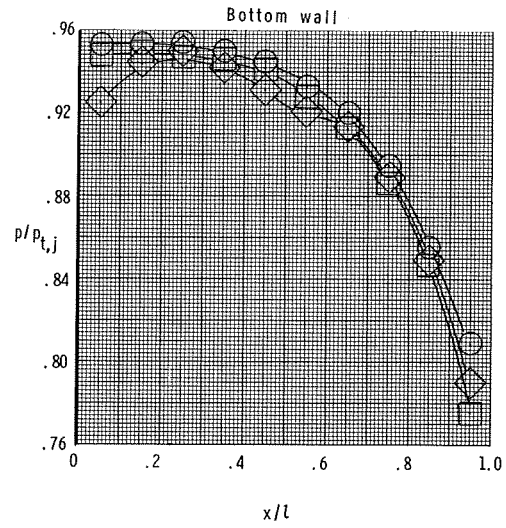
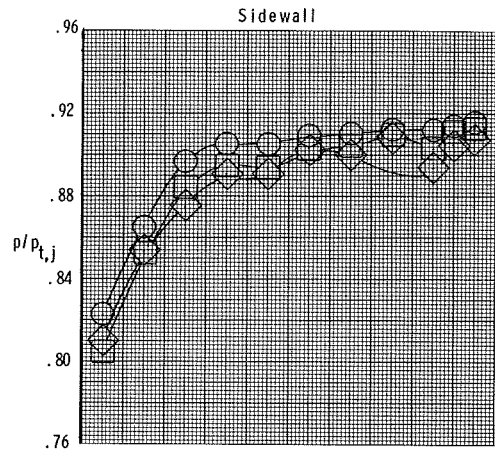


Figure 12. Effect of NPR on static-pressure ratios of lower half of transition section for configuration 4 with no induced swirl. Contour interval = 0.02.

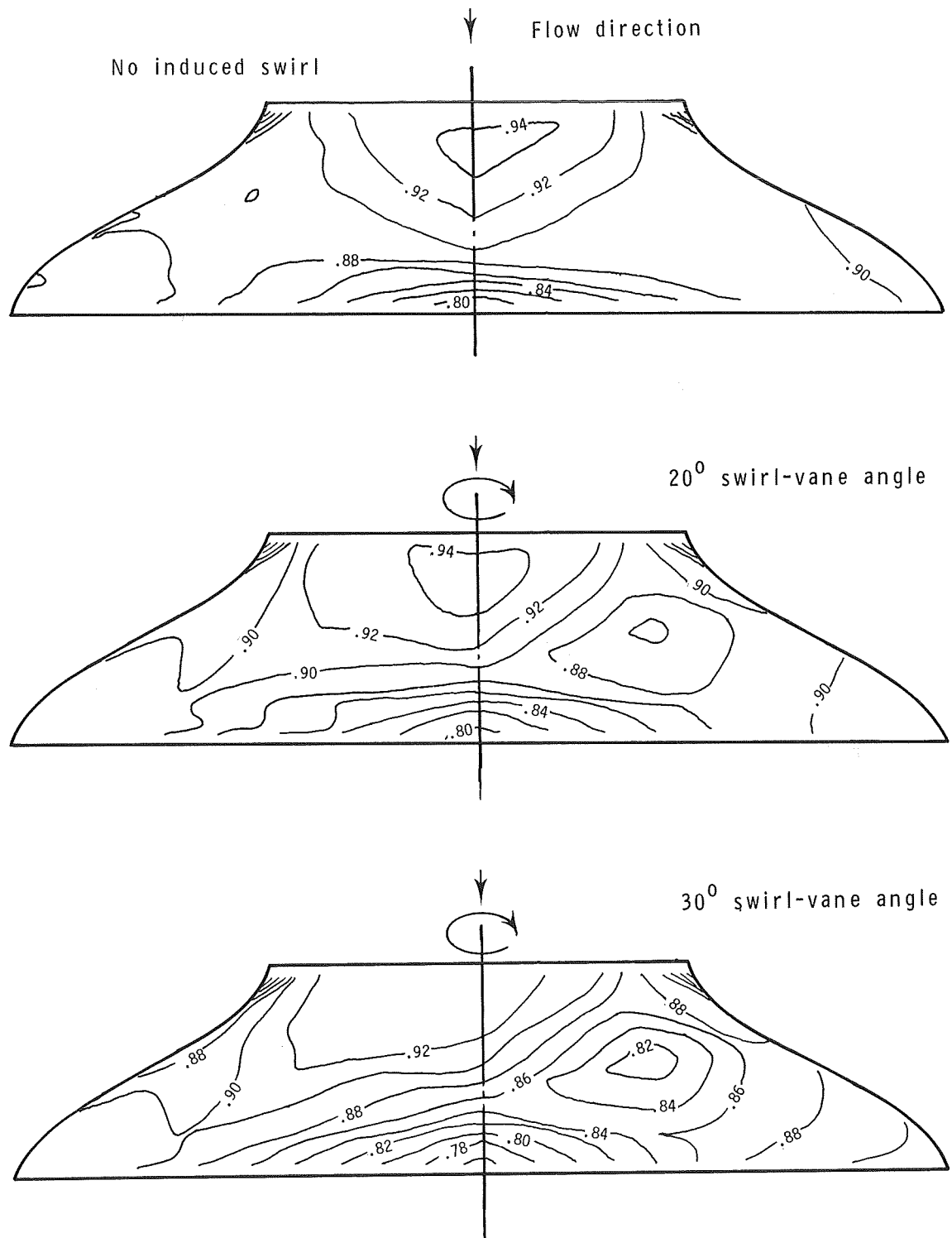
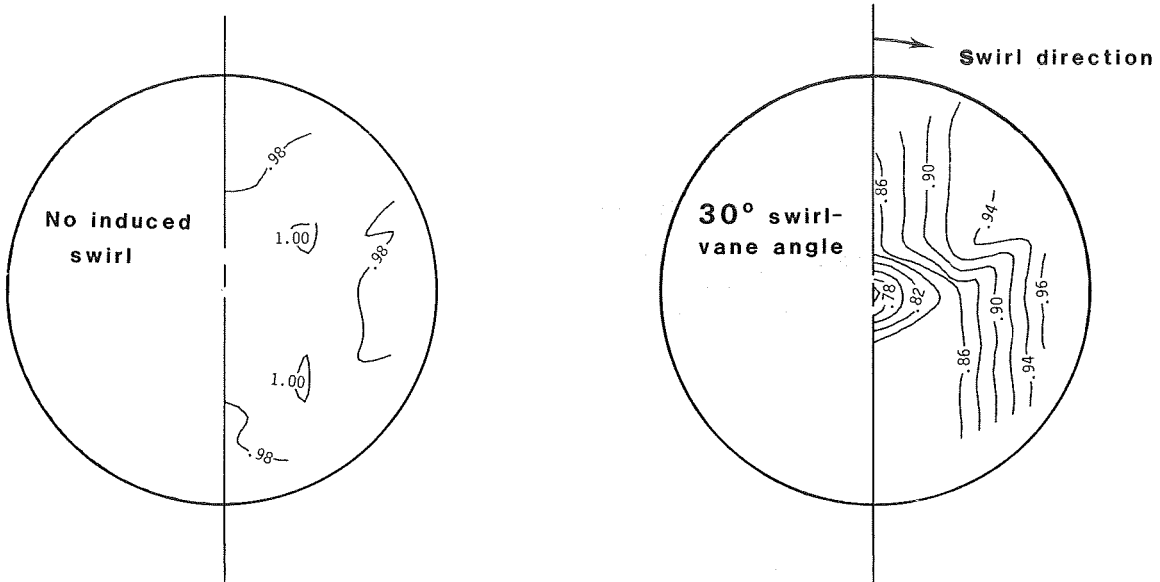


Figure 13. Effect of swirl-vane angle on static-pressure-ratio contours on lower half of configuration-4 transition duct. NPR = 4.24; Contour interval = 0.02.

**Transition entrance**

$x/l = -0.05$



**Transition exit**

$x/l = 1.05$

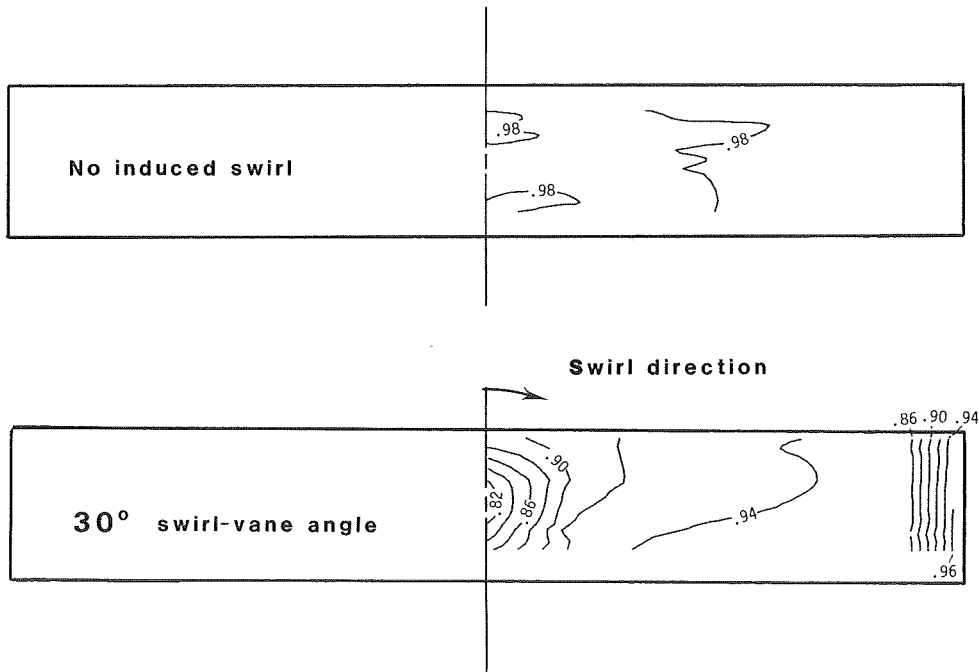


Figure 14. Contours of  $p_1/p_{t,j}$  at entrance and exit planes of configuration 2. NPR = 4.24; Contour interval = 0.02.

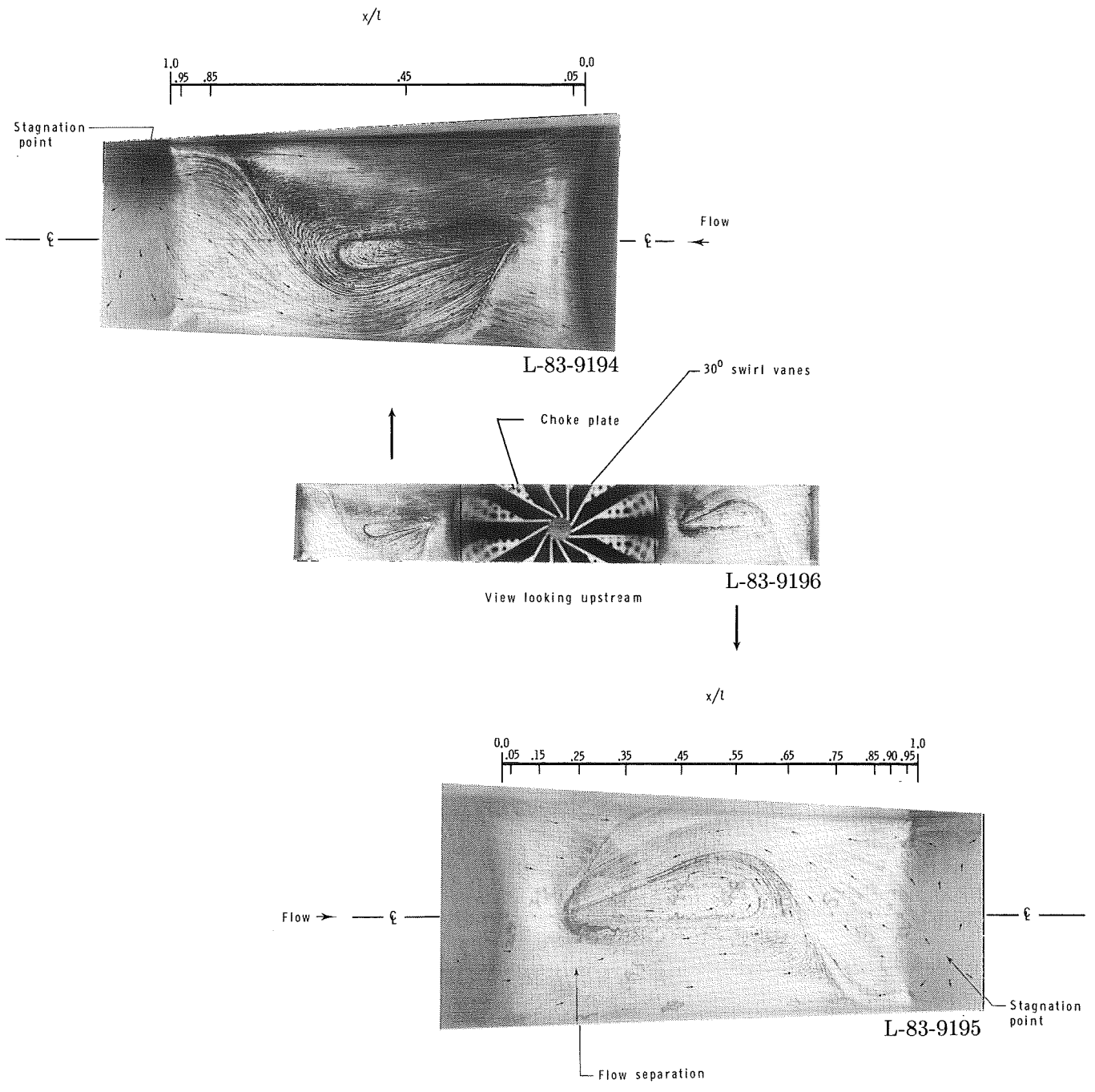
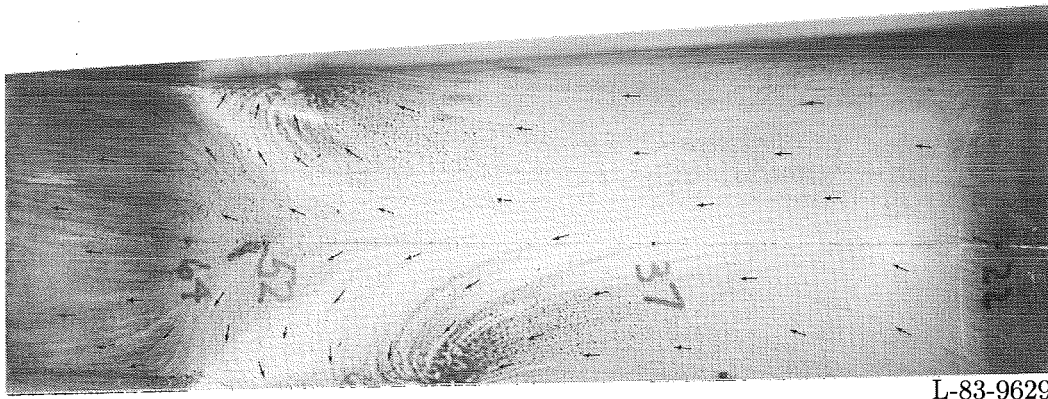
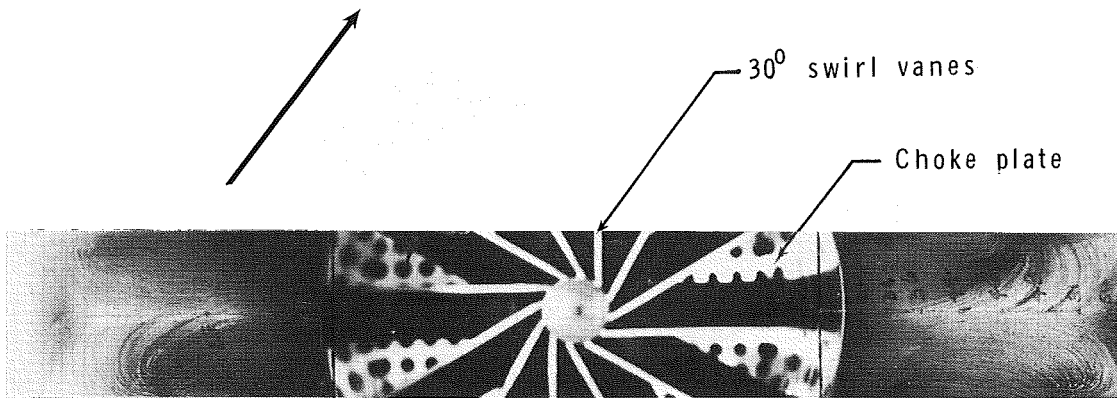


Figure 15. Oil-flow photographs of configuration 4 with 30° swirl vanes. Small arrows on photographs indicate observed flow direction.

ORIGINAL PAGE IS  
OF POOR QUALITY

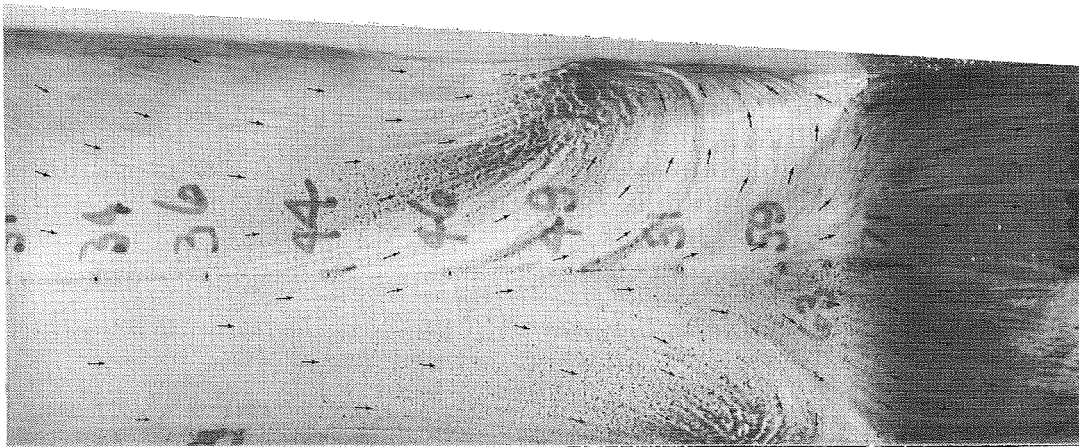


L-83-9629



View looking upstream

L-83-9628



L-83-9630

Figure 16. Oil-flow photographs of configuration 5 with 30° swirl vanes. Small arrows on photographs indicate observed flow direction.

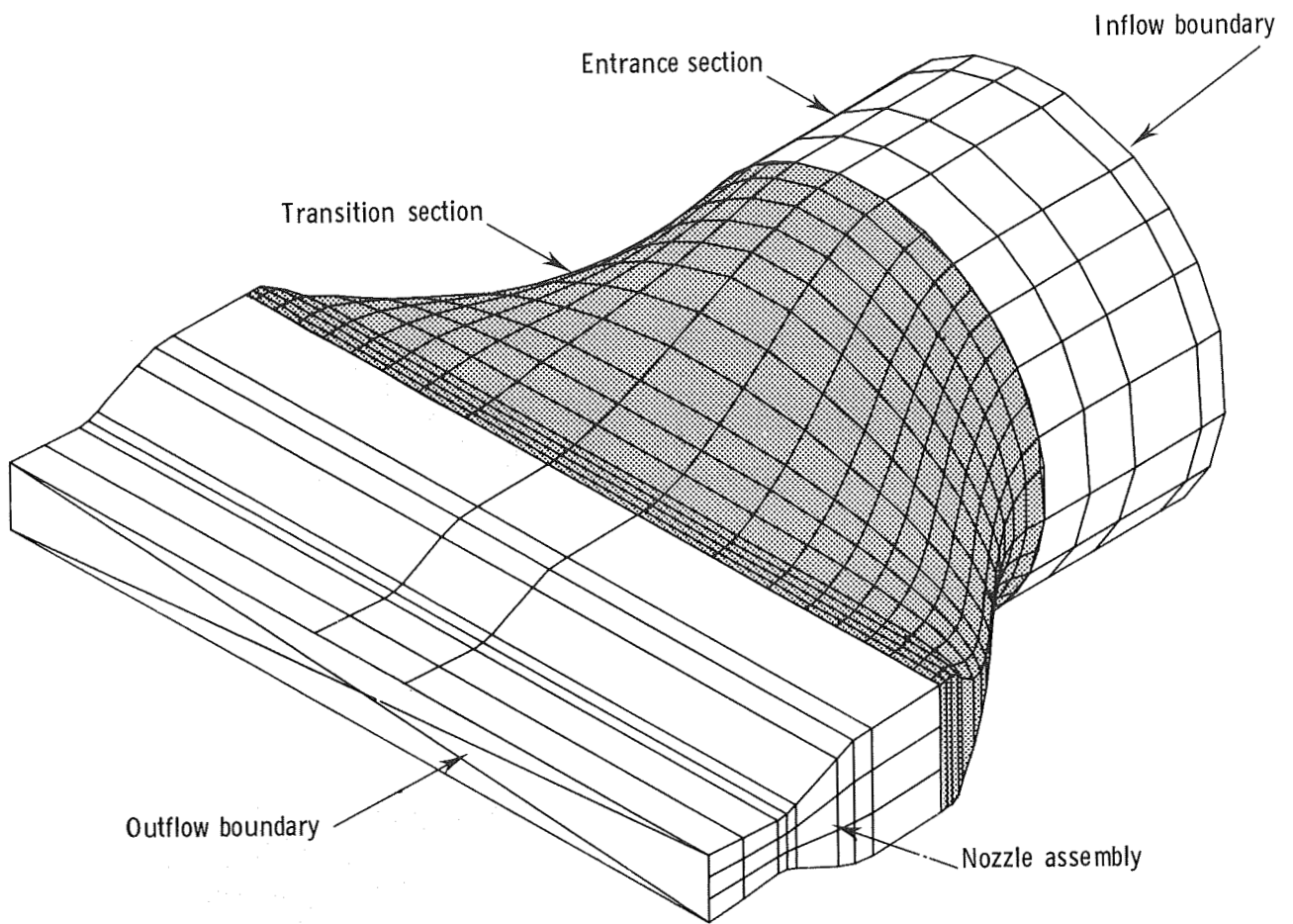


Figure 17. Numerical model of transition duct and nozzle for analysis code MCAERO.

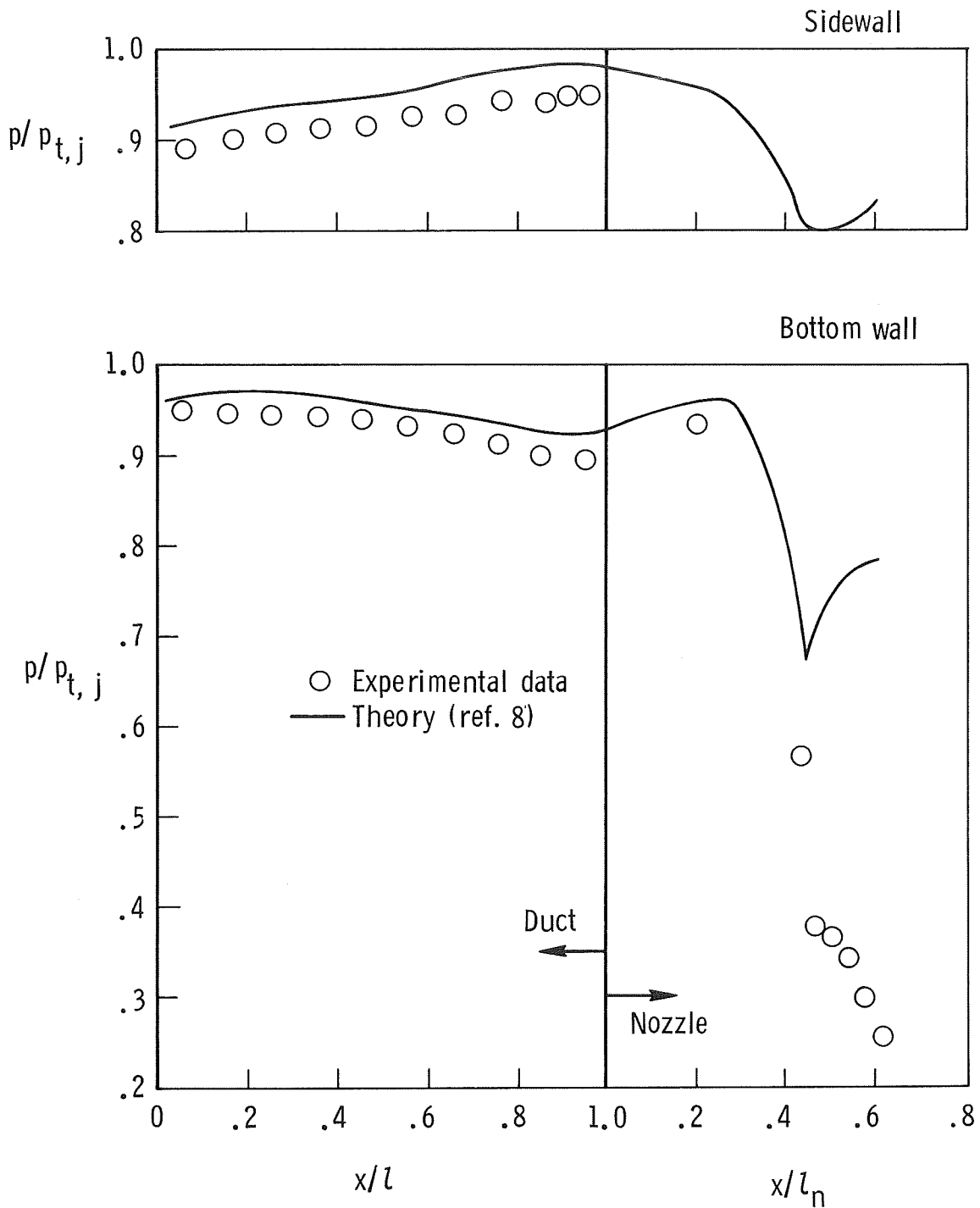


Figure 18. Comparison of experimental data and theoretical calculations of internal static-pressure ratios for transition duct 2. NPR = 4.00; no swirl.

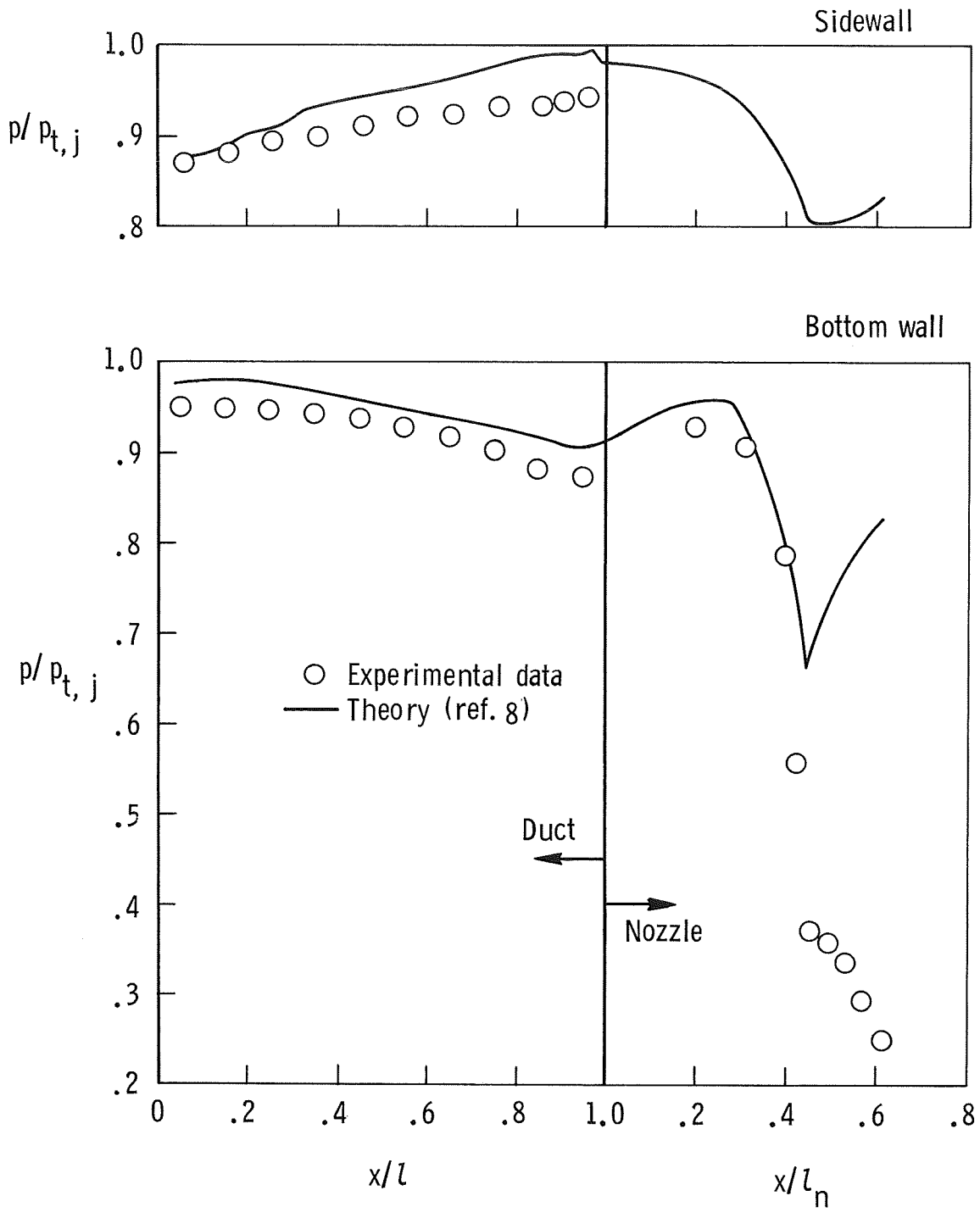


Figure 19. Comparison of experimental data and theoretical calculations of internal static-pressure ratios for transition duct 3. NPR = 4.00; no swirl.

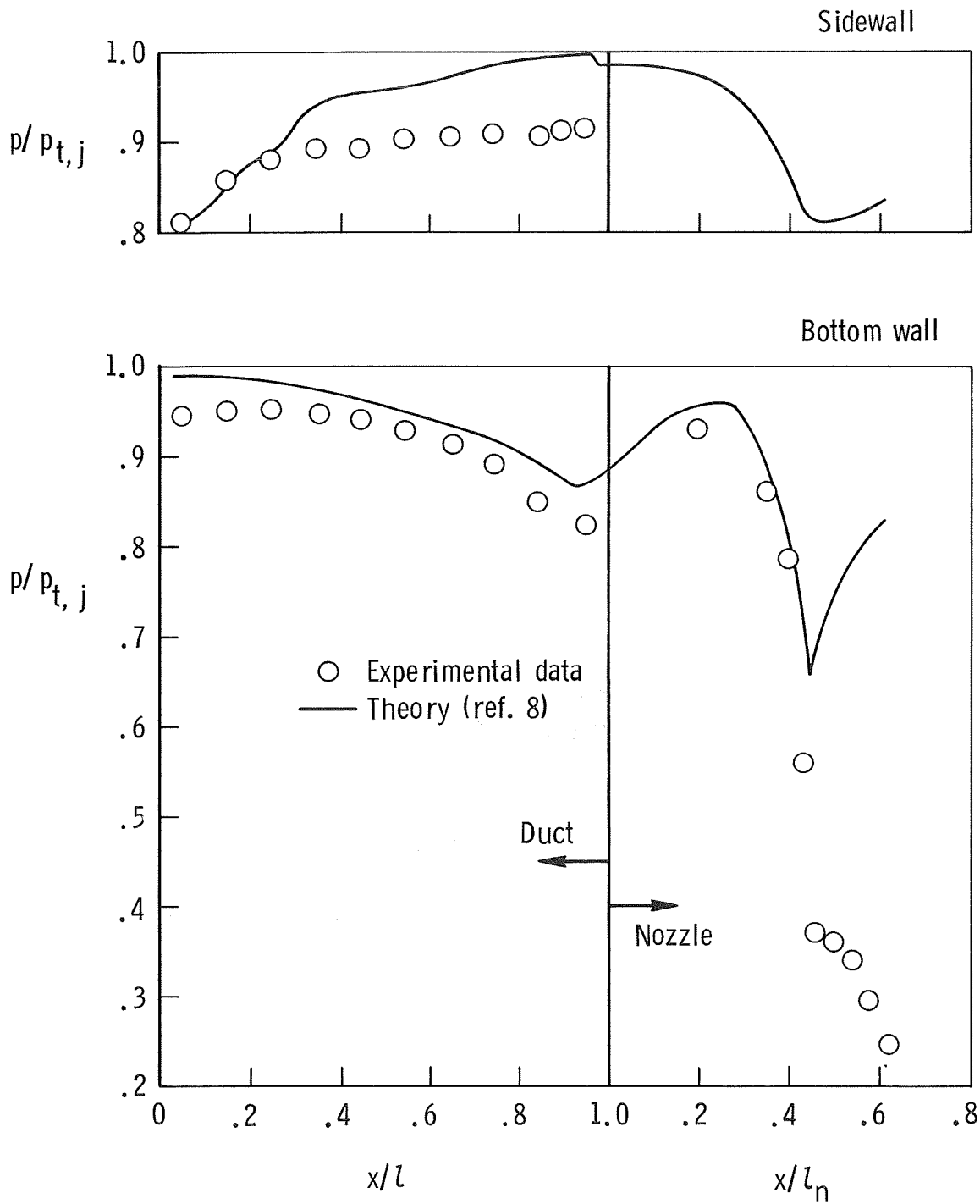


Figure 20. Comparison of experimental data and theoretical calculations of internal static-pressure ratios for transition duct 4. NPR = 4.00; no swirl.

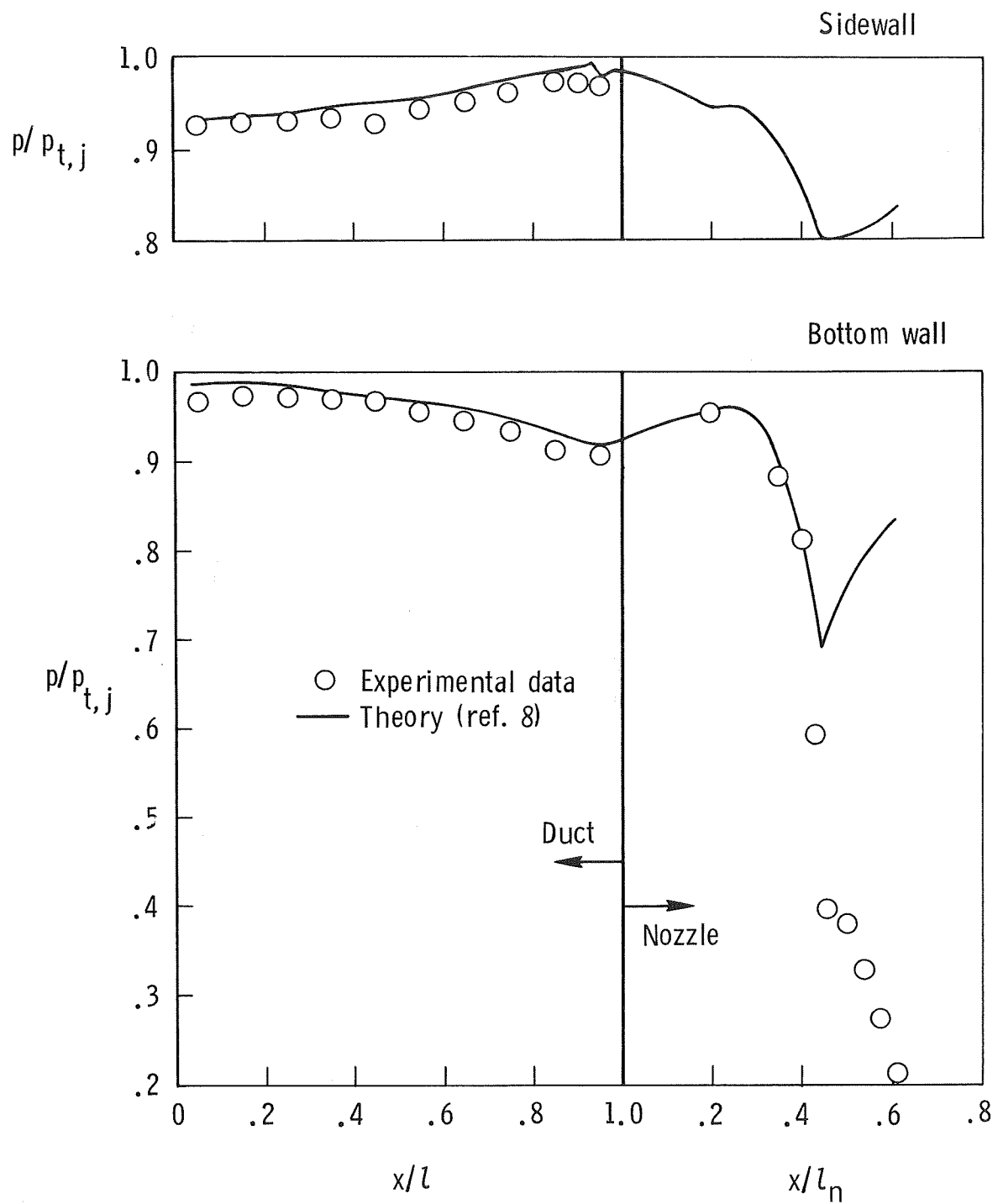


Figure 21. Comparison of experimental data and theoretical calculations of internal static-pressure ratios for transition duct 5. NPR = 4.00; no swirl.

1. Report No. NASA TP-2534	2. Government Accession No.	3. Recipient's Catalog No.	
4. Title and Subtitle Static Investigation of Circular-to-Rectangular Transition Ducts for High-Aspect-Ratio Nonaxisymmetric Nozzles		5. Report Date March 1986	
		6. Performing Organization Code 505-40-90-01	
7. Author(s) James R. Burley II, Linda S. Bangert, and John R. Carlson		8. Performing Organization Report No. L-15874	
		10. Work Unit No.	
9. Performing Organization Name and Address NASA Langley Research Center Hampton, VA 23665-5225		11. Contract or Grant No.	
		13. Type of Report and Period Covered Technical Paper	
12. Sponsoring Agency Name and Address National Aeronautics and Space Administration Washington, DC 20546-0001		14. Sponsoring Agency Code	
		15. Supplementary Notes Appendix by James R. Burley II, NASA Langley Research Center, Hampton, Virginia.	
16. Abstract An investigation was conducted in the static-test facility of the Langley 16-Foot Transonic Tunnel to determine the internal performance of a high-aspect-ratio nonaxisymmetric nozzle with five circular-to-rectangular transition ducts of varying design. Nozzle pressure ratio was varied from 1.5 to 5.3, and nozzle performance parameters were recorded.			
17. Key Words (Suggested by Authors(s)) Nozzle performance Nonaxisymmetric nozzle Transition duct Subsonic diffuser Superellipse		18. Distribution Statement Unclassified—Unlimited  Subject Category 07	
19. Security Classif.(of this report) Unclassified	20. Security Classif.(of this page) Unclassified	21. No. of Pages 53	22. Price A04

National Aeronautics and  
Space Administration  
Code NIT-4

Washington, D.C.  
20546-0001

Official Business  
Penalty for Private Use, \$300

BULK RATE  
POSTAGE & FEES PAID  
NASA  
Permit No. G-27

**NASA**

---

POSTMASTER: If Undeliverable (Section 158  
Postal Manual) Do Not Return